nature communications

Article

https://doi.org/10.1038/s41467-025-60226-1

Ferroptosis-activating metabolite acrolein antagonizes necroptosis and anti-cancer therapeutics

Received: 26 July 2024

Accepted: 19 May 2025

Hyun Bae[1,8], Seonghyun Moon[1,2,8], Mengmeng Chang[3], Fenfen Zhang[3], Yeonseo Jang[1], Wonyoung Kim[1], Soyeon Kim[1], Minjie Fu[1], Jaemin Lim[4], Seongjun Park[4], Chirag N. Patel[5,6], Raghvendra Mall[5], Min Zheng[3], Si Ming Man[7,9] & Rajendra Karki[1,9]

Dysregulated cell death leading to uncontrolled cell proliferation is a hallmark of cancer. Chemotherapy-induced cell death is critical for the success of cancer treatment but this process is impaired by metabolic byproducts. How these byproducts interfere with anti-cancer therapy is unclear. Here, we show that the metabolic byproduct acrolein derived from polyamines, tobacco smoke or fuel combustion, induces ferroptosis independently of ZBP1, while suppressing necroptosis in cancer cells by inhibiting the oligomerization of the necroptosis effector MLKL. Loss of the enzyme SAT1, which contributes to intracellular acrolein production, sensitizes cells to necroptosis. In mice, administration of an acrolein-trapping agent relieves necroptosis blockade and enhances the anti-tumor efficacy of the chemotherapeutic drug cyclophosphamide. Human patients with cancer coupled with a higher cell death activity but a lower expression of genes controlling polyamine metabolism exhibit improved survival. These findings highlight that the removal of metabolic byproducts improves the success of certain chemotherapies.

Cell death is a fundamental biological process crucial for eliminating damaged cells, maintaining tissue homeostasis, and regulating developmental processes. Regulated cell death (RCD) pathways characterized by distinct morphological, biochemical, and molecular features have been identified[1–3]. Pyroptosis is executed by gasdermin D (GSDMD) downstream of inflammasome signaling[4]. However, in cancer cells lacking GSDMD, pyroptosis can occur through gasdermin E (GSDME) following caspase-3 activation[5]. Apoptosis is activated by the extrinsic initiator caspase-8 or intrinsic initiator caspase-9, ultimately leading to activation of downstream executioners caspase-3, -6, and -7[6–8]. In the absence of caspase-8 activity, activation of receptor-interacting serine/threonine kinase (RIPK)1, RIPK3, and mixed lineage kinase domain-like pseudokinase (MLKL) leads to necroptosis[9–11]. Oxidative damage to cellular membranes by iron-dependent accumulation of lipid peroxides results in ferroptosis[12].

Agents that promote cell death are used extensively as chemotherapeutics in cancer treatment[13–15]. However, a major limitation in chemotherapy is drug resistance due to the evasion of apoptosis by cancer cells[16,17]. Necroptosis provides an alternative way to kill cancer cells, offering potential therapeutic avenues for therapy-resistant cancers[18,19].

---

[1]Department of Biological Sciences, College of Natural Sciences, Seoul National University, Seoul, Republic of Korea. [2]Department of Biology Education, College of Education, Seoul National University, Seoul, Republic of Korea. [3]Institute of infectious diseases, Shenzhen Bay Laboratory, Shenzhen, Guangdong, China. [4]Bertis Inc., Gyeonggi-do, Republic of Korea. [5]Biotechnology Research Center, Technology Innovation Institute, Abu Dhabi, UAE. [6]Translational Gerontology Branch, National Institute on Aging, NIH, Baltimore, MD, USA. [7]Division of Immunology and Infectious Diseases, The John Curtin School of Medical Research, The Australian National University, Canberra, Australia. [8]These authors contributed equally: Hyun Bae, Seonghyun Moon. [9]These authors jointly supervised this work: Si Ming Man, Rajendra Karki. e-mail: siming.man@anu.edu.au; rkarki@snu.ac.kr

Cellular metabolites and drug byproducts often complicate chemotherapy efficacy with poorly defined molecular mechanisms[20–23]. The polyamine metabolic pathway is considered a rational target for therapeutic intervention; however, mixed responses have been observed in both clinical and preclinical settings[24]. Polyamines, such as spermine, spermidine, and their precursor putrescine, control fundamental biological processes, including transcription, translation, and cell signaling[24]. Polyamine catabolism, mediated by intracellular enzymes such as spermidine/spermine N^1-acetyltransferase 1 (SAT1, also known as diamine acetyltransferase 1), polyamine oxidases, and spermine oxidase (SMOX), yields toxic metabolites including acrolein and hydrogen peroxide that may drive cell death[25–29]. However, how polyamine metabolism triggers cell death activities and how this relationship affects the survival and treatment outcome of cancer patients have remained unclear.

In this study, we observe that spermine and spermidine induce cell death, with the metabolic byproduct acrolein triggering lipid peroxidation and ferroptosis. Cells treated with acrolein do not undergo necroptotic cell death even in the presence of phosphorylation of RIPK3 and MLKL, owing to the role of acrolein in blocking MLKL oligomerization. Similarly, deletion of the enzyme SAT1 involved in generating acrolein intracellularly, renders cells susceptible to necroptosis. Removal of acrolein and liberation of necroptosis enhance the efficacies of chemotherapeutics in cells and mice. Overall, our results suggest that barriers imposed by toxic host metabolites against certain chemotherapeutic drugs can be removed to enhance treatment outcome.

Results

Spermine induces inflammatory lytic cell death ferroptosis

Natural polyamines such as spermine are found ubiquitously in organisms from all kingdoms and can intersect with regulated cell death (RCD) pathways[25–29]. We treated primary bone marrow-derived macrophages (BMDMs) with varying concentrations of spermine to monitor the kinetics of cell death and found that spermine concentrations at 25 µM or higher induced robust cell death (Fig. 1A, B). To comprehensively understand this phenomenon across multiple cell types in mice and humans, we used spermine to stimulate primary mouse BMDMs, immortalized mouse BMDMs (iBMDMs), mouse fibroblast cell line L929, mouse colorectal cancer cell line CT-26, human colorectal cancer cell line HT-29, human renal cancer cell lines Caki-1 and A498, and human lung cancer cell line A549. Only primary mouse BMDMs and iBMDMs exhibited susceptibilities to spermine-induced cell death, whereas mouse cell lines L929 and CT-26 remained resistant (Supplementary Fig. 1A, B). In human cell lines, only Caki-1 cells succumbed to cell death in response to spermine stimulation (Supplementary Fig. 1C–E). Stimulation of BMDMs with spermine led to the release of cytosolic contents such as lactate dehydrogenase (LDH) and high mobility group box 1 (HMGB1) (Fig. 1C)[30,31], indicating that spermine induces lytic inflammatory cell death.

We next sought to characterize the nature of cell death induced by spermine. Of the regulated cell death pathways, pyroptosis, necroptosis, and ferroptosis are lytic, each with their unique molecular signatures[12,32–36]. Treatment of BMDMs with spermine did not induce the proteolytic cleavage of caspase-1, GSDMD or GSDME (Supplementary Fig. 1F), indicating the lack of pyroptosis or inflammasome activation. Additionally, we saw a lack of caspase-3, -7, or -8 cleavage (Supplementary Fig. 1G), suggesting that apoptosis is not involved. BMDMs stimulated with spermine underwent the phosphorylation of RIPK3 and MLKL, and the magnitude of phosphorylation increased with increased length of stimulation time and concentrations of spermine (Fig. 1D, E), leading to LDH and HMGB1 release (Fig. 1F). The activation of RIPK3 and MLKL by spermine indicates hallmarks of necroptosis. The RIPK1 inhibitor, necrostatin-1 (Nec-1)[10] effectively abolished necroptosis induced by the classical combination of TNF, Smac mimetic, and Z-VAD-FMK (zVAD), referred to as TSZ herein (Supplementary Fig. 2A, B)[11]. However, Nec-1 only partially inhibited spermine-induced cell death and the release of LDH and HMGB1 (Fig. 1G, H), indicating that necroptosis cannot fully account for the magnitude of cell death.

To validate our findings using a genetic approach, we treated *Ripk3*$^{-/-}$ and *Mlkl*$^{-/-}$ BMDMs, which are defective in necroptosis, with spermine. Surprisingly, *Ripk3*$^{-/-}$ and *Mlkl*$^{-/-}$ BMDMs were susceptible to spermine-induced cell death (Supplementary Fig. 2C–E), suggesting that necroptosis is not involved and that the partial resistance to cell death caused by Nec-1-mediated RIPK1 blockade might be an off-target effect. In line with previous reports that Nec-1 can inhibit ferroptosis in a RIPK1-independent manner[37,38], we observed that Nec-1 partially inhibited ferroptotic cell death induced by ras-selective lethal small molecule 3 (RSL3), a glutathione peroxidase 4 (GPX4) inhibitor (Supplementary Fig. 2F)[39]. Similarly, Nec-1 attenuated the release of LDH and HMGB1 in BMDMs treated with RSL3 or spermine (Supplementary Fig. 2G). These data indicate that spermine may induce ferroptosis that is partially attenuated by Nec-1. Indeed, we observed that BMDMs treated with spermine or RSL3 both showed increased lipid peroxide accumulation seen in ferroptosis (Fig. 2A, B). Moreover, treatment with the lipid-peroxidation inhibitor Fer-1 abolished the accumulation of lipid peroxides (Fig. 2A, B), cell death (Fig. 2C, D), and the release of LDH and HMGB1 (Fig. 2E) in BMDMs stimulated with spermine or RSL3. Fer-1 also blocked cell death in the human renal cancer cell line Caki-1 stimulated with spermine (Supplementary Fig. 2H). Since the extent of cell death by ferroptosis depends on cell density[40], we next examined the effects of cell density in spermine-induced cell death. Notably, mouse BMDMs or human Caki-1 cells stimulated with spermine exhibited density-dependent cell death, with highly confluent cells failing to undergo ferroptosis, similar to BMDMs stimulated with RSL3 (Supplementary Fig. 3A–C).

To address the potential crosstalk between spermine-induced ferroptosis and the phosphorylation of RIPK3 and MLKL, we treated BMDMs with spermine in the presence of Fer-1 or Nec-1. Despite fully or partially mitigating cell death induced by spermine, neither Fer-1 nor Nec-1 inhibited the phosphorylation of RIPK3 and MLKL (Figs. 1G and 2C, F and G). This finding implies that while spermine induces the activation of RIPK3 and MLKL, these events do not contribute to cell death. In contrast, BMDMs stimulated with RSL3 secreted LDH and HMGB1 but had minimal phosphorylation of RIPK3 and MLKL (Fig. 2F–I). Consistent with the observation from spermine treatment, neither genetic deletion of MLKL nor pharmacological inhibition of RIPK3 with GSK blocked RSL3-induced cell death (Supplementary Fig. 3D). Similarly, Fer-1 treatment did not inhibit TSZ-induced cell death (Supplementary Fig. 3E). Collectively, these findings suggest that ferroptosis and necroptosis, executed under our experimental conditions, are distinct and independent cell death pathways.

Spermine-induced ferroptosis is mediated by the metabolite acrolein

Spermine is biochemically converted to another polyamine called spermidine and subsequently to the polyamine putrescine[41]. To explore whether polyamines other than spermine can induce cell death, we treated BMDMs with spermidine, putrescine, and their precursor ornithine, and monitored for cell death. Only spermidine triggered cell death (Supplementary Fig. 4A–C), suggesting that spermine and spermidine may share a common cell death-inducing mechanism.

Both spermine and spermidine produce toxic metabolites including acrolein and hydrogen peroxide (H_2O_2) as byproducts following oxidation by bovine serum amine oxidase present in fetal bovine serum (FBS) of cell culture systems[42]. Therefore, we examined the contribution of acrolein and H_2O_2 in triggering ferroptosis using the acrolein quencher hydralazine, or free radical scavengers of H_2O_2,

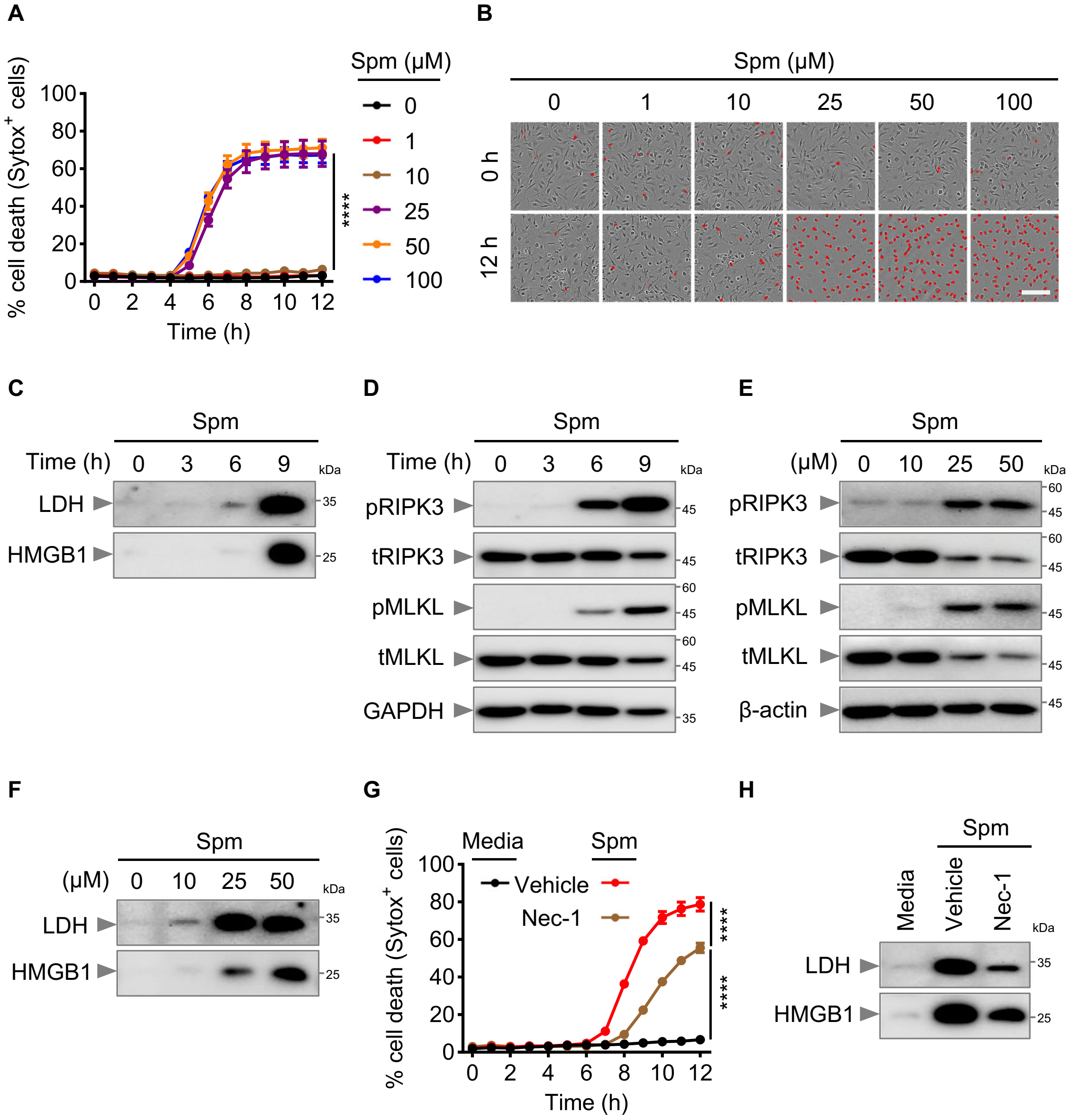

Fig. 1 | Spermine triggers inflammatory cell death and activates necroptotic molecules. **A** Real-time analysis of cell death in bone marrow-derived macrophages (BMDMs) treated with different doses of spermine (Spm). **B** Representative images of cell death in BMDMs at 0 and 12 h of indicated doses of Spm treatment. **C**, **D** Immunoblot analysis of (**C**) released lactate dehydrogenase (LDH) and high mobility group box 1 (HMGB1) in the cell culture media; (**D**) phosphorylated receptor-interacting serine/threonine kinase 3 (pRIPK3), total RIPK3 (tRIPK3), phosphorylated mixed lineage kinase domain-like pseudokinase (pMLKL), and total MLKL (tMLKL) after indicated times of Spm treatment. GAPDH was used as internal control. **E**, **F** Immunoblot analysis of (**E**) pRIPK3, tRIPK3, pMLKL, and tMLKL; (**F**) released LDH and HMGB1 in the cell culture media in BMDMs after indicated doses of Spm treatment. β-actin was used as an internal control (**E**). **G** Real-time analysis of cell death in BMDMs treated with Spm in the presence or absence of necrostatin-1 (Nec-1). **H** Immunoblot analysis of released LDH and HMGB1 in the cell culture media after indicated treatments in BMDMs. Data are shown as mean ± SEM; ****$P < 0.0001$ (two-way ANOVA; $n = 4$ from 4 biologically independent samples) (**A** and **G**). Data are representative of at least three independent experiments (**B**–**F** and **H**). Scale bar, 100 μm (**B**). Source data are provided as a Source Data file.

sodium pyruvate, and dimethylthiourea[43–45]. Both sodium pyruvate and dimethylthiourea effectively scavenged H_2O_2 in the presence of spermine under cell culture conditions (Supplementary Fig. 4D). Remarkably, BMDMs treated with hydralazine, but not sodium pyruvate or dimethylthiourea, were resistant to spermine-induced cell death (Fig. 3A) and had reduced accumulation of lipid peroxides (Fig. 3B), suggesting that spermine-induced cell death is mediated by acrolein. Further, acrolein stimulation killed BMDMs (Fig. 3C) and induced lipid peroxidation (Fig. 3D), both of which were attenuated by Fer-1 and hydralazine, but not by sodium pyruvate or dimethylthiourea (Fig. 3D, E). Similarly, acrolein-induced cell death was inhibited by Fer-1 in Caki-1 human renal cancer cells (Supplementary Fig. 4E, F). To further confirm the role of H_2O_2 in polyamine-induced cell death, BMDMs were treated with different concentrations of exogenous H_2O_2. Lower concentrations of H_2O_2 failed to induce cell death, whereas higher concentrations of H_2O_2 triggered cell death that was not inhibited by Fer-1 (Supplementary Fig. 4G). This observation indicates that high-dose H_2O_2-induced cell death occurs via a non-ferroptotic mechanism. While H_2O_2 did not directly contribute to polyamine-induced cell death under our experimental conditions, polyamines have previously been shown to enhance cellular sensitivity to RSL3-induced ferroptosis through H_2O_2 generation[46]. Consistently, a moderate dose of exogenous H_2O_2 accelerated RSL3-induced cell death (Supplementary Fig. 4H).

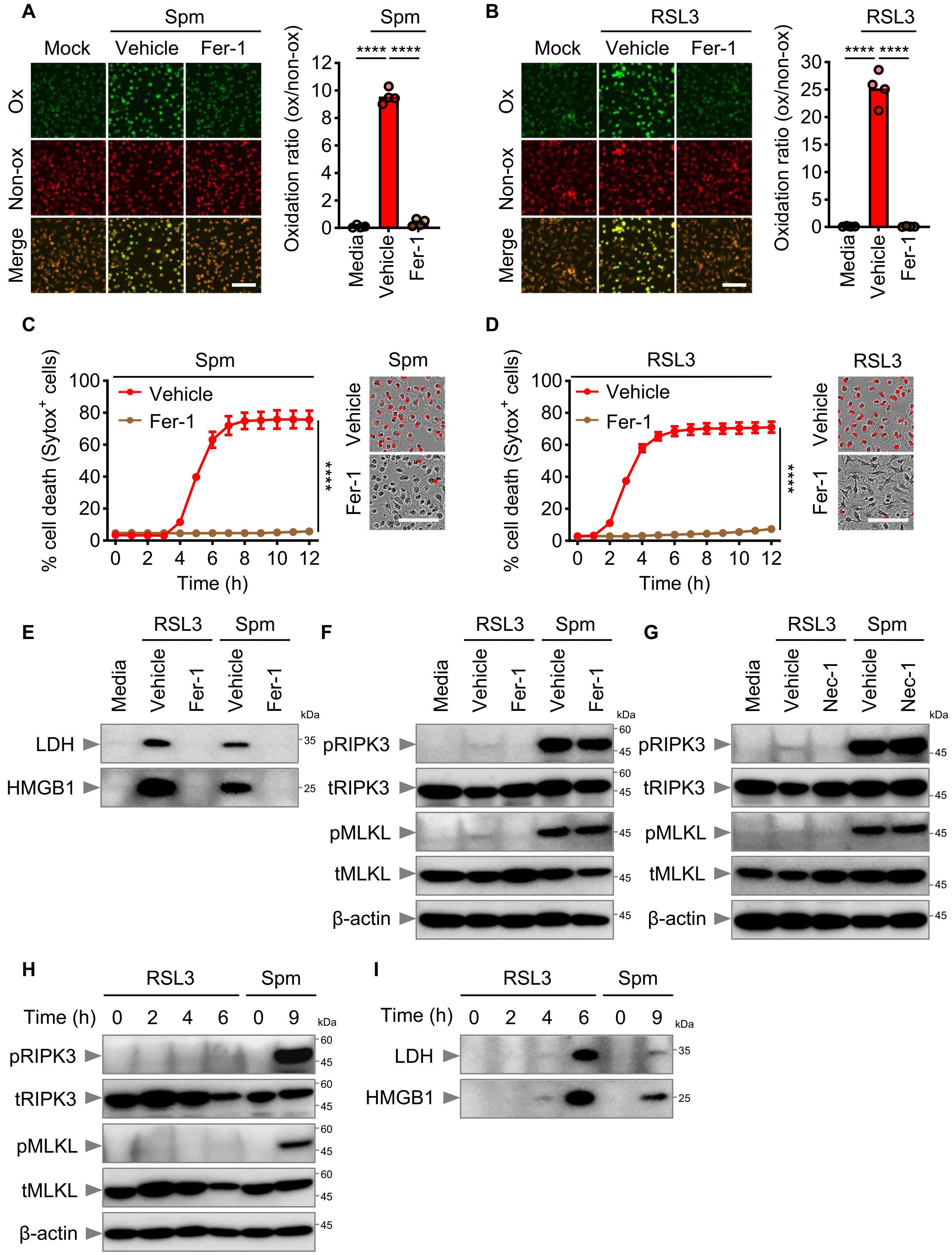

We further investigated whether the breakdown of spermine or spermidine by amine oxidase found in FBS potentiated the production of ferroptosis-inducing acrolein. To this end, we treated BMDMs with spermine or spermidine in the absence or presence of FBS. Remarkably, both spermine and spermidine did not induce ferroptosis in the absence of FBS (Supplementary Fig. 5A, B), whereas RSL3 induced ferroptosis in the absence or presence of FBS (Supplementary Fig. 5C). Further, we substituted FBS with human serum that contains a low-level of amine oxidase[47]. Spermine and spermidine did not induce cell death in BMDMs cultured with human serum, whereas RSL3-induced cell death was unaffected (Supplementary Fig. 5D–F). Additionally, pre-incubation of spermine and spermidine, but not RSL3, with FBS-containing media accelerated the kinetics of cell death (Supplementary Fig. 5G–I). Consistent with the phenomenon observed with

Fig. 2 | Ferroptosis inhibition abolishes spermine-induced cell death without altering the activation of RIPK3 and MLKL. A, B Representative images of oxidized lipids (green) and non-oxidized lipids (red) with merged images and oxidation ratio in BMDMs treated with (**A**) spermine (Spm) for 9 h; (**B**) ras-selective lethal small molecule 3 (RSL3) for 6 h. **C, D** Real-time analysis and representative images of cell death in BMDMs treated with (**C**) Spm; (**D**) RSL3 for 6 h in the presence or absence of ferrostatin-1 (Fer-1). **E** Immunoblot analysis of released lactate dehydrogenase (LDH) and high mobility group box 1 (HMGB1) in cell culture media of BMDMs stimulated with RSL3 and Spm in the presence or absence of Fer-1. **F, G** Immunoblot analysis of phosphorylated receptor-interacting serine/threonine kinase 3 (pRIPK3), total RIPK3 (tRIPK3), phosphorylated mixed lineage domain-like pseudokinase (pMLKL), and total MLKL (tMLKL) in BMDMs treated with RSL3 and spermine in the presence or absence of (**F**) Fer-1; (**G**) necrostatin-1 (Nec-1). **H** Immunoblot analysis of pRIPK3, tRIPK3, pMLKL, and tMLKL in BMDMs after indicated times of RSL3 and Spm treatment. β-actin was used as an internal control (**F–H**). **I** Immunoblot analysis of released LDH and HMGB1 in the cell culture media of BMDMs after indicated times of RSL3 and Spm treatment. Data are shown as mean ± SEM (**A–D**). $^{****}P < 0.0001$ (one-way ANOVA; $n = 4$ from 4 biologically independent samples) (**A** and **B**). $^{****}P < 0.0001$ (two-tailed t test; $n = 4$ from 4 biologically independent samples) (**C** and **D**). Data are representative of at least three independent experiments (**A–I**). Scale bar, 100 μm (**A–D**). Source data are provided as a Source Data file.

spermine, neither Nec-1 nor Fer-1 treatment altered acrolein-induced phosphorylation of RIPK3 and MLKL (Supplementary Fig. 6A), whereas cell death was abolished by Fer-1 (Fig. 3E) and partially attenuated by Nec-1 (Supplementary Fig. 6B). Collectively, these findings indicate that polyamine-induced ferroptosis is mediated by acrolein generated from polyamine catabolism.

ZBP1, inflammasomes and type I IFN signaling are not required for acrolein-induced ferroptosis

Oxidative stressors have been reported to induce endogenous Z-RNA accumulation[48,49]. Acrolein is known to induce oxidative stress[50], which might induce Z-RNA accumulation and cell death. Moreover, spermine and spermidine cause the transition of B-DNA to Z-DNA. Both Z-RNA and Z-DNA binds to the innate immune sensor ZBP1 to trigger cell death[51–54]. Indeed, we observed that spermine or acrolein-induced Z-RNA accumulation in BMDMs (Fig. 4A–C). However, *Zbp1*$^{-/-}$ or *Zbp1*$^{\Delta Z\alpha 2}$ (lacking the nucleic-acid binding Zα2 domain) BMDMs stimulated with spermine or acrolein showed a similar magnitude of cell death compared with wild-type (WT) BMDMs (Fig. 4D–G), suggesting that ZBP1 is dispensable for polyamine-induced ferroptosis. Further, *Zbp1*$^{-/-}$ BMDMs with or without Nec-1 treatment underwent RIPK3 and MLKL phosphorylation, similar to WT BMDMs in response to spermine or acrolein (Fig. 4H, I). BMDMs lacking inflammasome sensors or components that control cell death[55,56] (*Nlrp3*$^{-/-}$, *Aim2*$^{-/-}$, *Nlrc4*$^{-/-}$, *Mefv*$^{-/-}$, and *Casp1*$^{-/-}$ BMDMs), type I IFN signaling (*Ifnar1*$^{-/-}$ BMDMs), or STING (*Sting*$^{-/-}$ BMDMs) all succumbed to ferroptosis induced by spermine or acrolein (Supplementary Fig. 7). These results highlight that acrolein induces the accumulation of Z-RNA and ferroptosis, but ZBP1, inflammasomes and type I IFN signaling pathways do not contribute to acrolein-induced ferroptosis.

Protein modifications by acrolein induce ferroptosis

Acrolein irreversibly modifies proteins by forming covalent adducts with nucleophilic residues, such as cysteine, histidine, and lysine, significantly altering their structure and function, and potentially leading to cell death[57]. To investigate the effect of acrolein on cellular pathways, we performed chemoproteomic analysis of BMDMs treated with 50 μM acrolein for 1 h. A total of 1262 proteins were identified as targets of acrolein, and 51 proteins were associated with ferroptosis (Supplementary Datas 1 and 2 and Supplementary Fig. 8A). Within the ferroptosis pathway, acrolein-modified proteins included 28 drivers and 26 suppressors of ferroptosis (Supplementary Fig. 8A and Supplementary Data 2). Most of these proteins are known to regulate lipid oxidation and iron metabolism (Supplementary Data 2), which are critical processes in ferroptotic cell death[58]. Notably, we identified several acrolein-modified proteins that are well-known to be associated with ferroptosis, including acyl-CoA synthetase long chain family member 4 (ACSL4), heme oxygenase 1 (HMOX1), ferritin heavy chain 1 (FTH1), solute carrier family 3 member 2 (SLC3A2), peroxiredoxin 1 (PRDX1), and thioredoxin (TXN) (Supplementary Data 2)[59].

Among the identified targets, ferritin heavy chain 1 (FTH1) was highlighted as both a suppressor and a marker of ferroptosis (Supplementary Data 2). FTH1 plays a pivotal role in suppressing ferroptosis by maintaining intracellular iron homeostasis[60]. Acrolein adduction to FTH1 likely disrupts this function, increasing the intracellular labile iron pool and thereby sensitizing cells to ferroptosis. To assess the role of iron chelation in protecting against cell death, we treated cells with the iron chelator deferoxamine (DFO)[60]. DFO partially inhibited cell death induced by spermine, spermidine or acrolein (Supplementary Fig. 8B–D), suggesting that iron dysregulation contributes to acrolein-induced ferroptosis. However, the partial protection by the iron chelator indicates additional factors may also be involved. Indeed, the expression of key antioxidant proteins, including GPX4 and TXN1, was reduced following acrolein treatment in both BMDMs (Supplementary Fig. 8E) and Caki-1 cells (Supplementary Fig. 8F). Taken together, these data suggest that acrolein induces ferroptosis by modifying specific target proteins within the ferroptotic pathway, particularly those involved in lipid peroxidation and iron metabolism. These modifications, in conjunction with reductions in antioxidant defenses, highlight a multifaceted mechanism by which acrolein promotes ferroptotic cell death.

Acrolein inhibits MLKL oligomerization and necroptosis

Given that acrolein robustly induced the phosphorylation of RIPK3 and MLKL (Supplementary Fig. 6A) but still unable to trigger necroptosis, we hypothesized that acrolein might inadvertently impede necroptosis. Phosphorylated MLKL undergoes oligomerization, a critical step for the translocation of MLKL to cellular membranes, culminating in membrane permeabilization and necroptosis[61]. Considering the ability of acrolein to form adducts with various amino acid residues[57] potentially affecting appropriate assembly and trafficking, we postulated that acrolein impedes MLKL oligomerization. We observed that classical triggers of necroptosis, TSZ, induced MLKL phosphorylation and MLKL oligomer formation both in BMDMs and L929 cells, which were mitigated by Nec-1 (Fig. 5A and Supplementary Fig. 9A). Additionally, MLKL oligomers induced by TSZ dissociated following 1,4-dithiothreitol treatment (Fig. 5A). However, despite the induction of MLKL phosphorylation, cells treated with acrolein did not exhibit MLKL oligomer formation (Fig. 5A and Supplementary Fig. 9A). Since acrolein inhibited MLKL oligomerization, we sought to explore whether acrolein hindered cell death induced by necroptotic triggers. To overcome the ferroptosis-inducing effects of acrolein, we assessed whether acrolein prevented TSZ-induced necroptosis in BMDMs treated with Fer-1. Acrolein treatment inhibited MLKL oligomerization induced by TSZ in Fer-1-treated BMDMs (Fig. 5B). Furthermore, necroptosis induced by TSZ under this condition was abolished by acrolein (Fig. 5C). Similar findings were observed in ferroptosis-resistant human and mouse cancer lines (Fig. 5D–F and Supplementary Fig. 9B). To further investigate the intracellular dynamics of MLKL molecules in response to acrolein, we performed immunofluorescence staining and saw that TSZ, but not acrolein, induced localization of MLKL to the plasma membrane (Fig. 5G). Furthermore, acrolein inhibited plasma membrane localization of MLKL in TSZ-treated cells (Fig. 5G). To investigate whether intracellular polyamine metabolism affects necroptosis, we examined the role of the enzyme SAT1, a substantial contributor to the polyamine catabolic pathway[25]. WT and

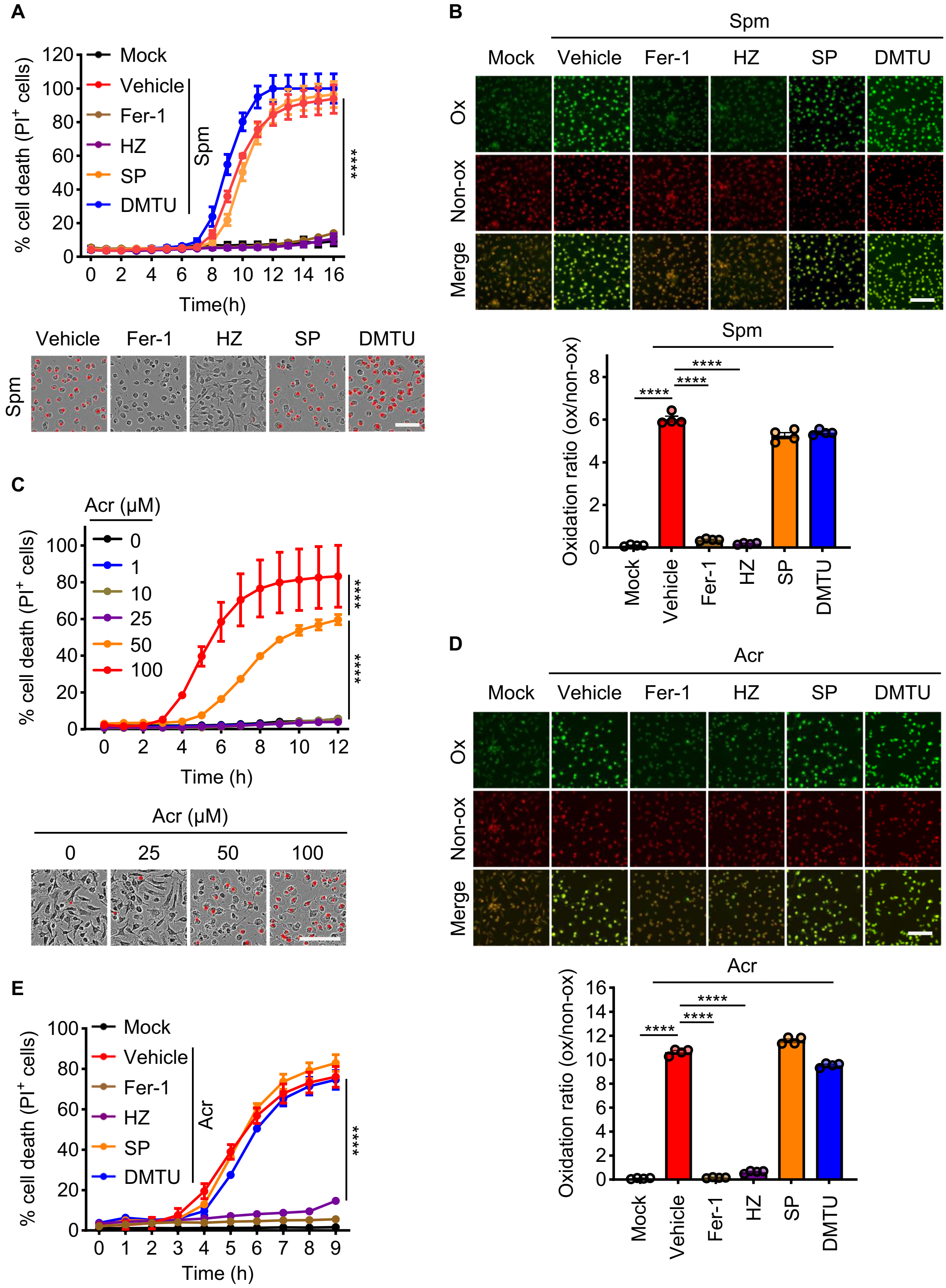

Fig. 3 | Spermine-induced ferroptosis is dependent on acrolein. A Real-time analysis and representative images of cell death in bone marrow-derived macrophages (BMDMs) treated with spermine (Spm) in the presence or absence of ferrostatin-1 (Fer-1), hydralazine (HZ), sodium pyruvate (SP), and dimethylthiourea (DMTU). **B** Representative images of oxidized lipids (green) and non-oxidized lipids (red) with merged images and oxidation ratio in BMDMs treated with Spm for 12 h in the presence or absence of Fer-1, HZ, SP, and DMTU. **C** Real-time analysis and representative images of cell death in BMDMs treated with different doses of acrolein (Acr). **D** Representative images of oxidized lipids (green) and non-oxidized lipids (red) with merged images and oxidation ratio in BMDMs treated with Acr for 6 h in the presence or absence of Fer-1, HZ, SP, and DMTU. **E** Real-time analysis of cell death in BMDMs stimulated with Acr in the presence or absence of Fer-1, HZ, SP, and DMTU. Data are shown as mean ± SEM (**A**–**E**). ****$P < 0.0001$ (two-way ANOVA; $n = 4$ from 4 biologically independent samples) (**A**, **C**, and **E**). ****$P < 0.0001$ (one-way ANOVA; $n = 4$ from 4 biologically independent samples) (**B** and **D**). Data are representative of at least three independent experiments (**B** and **D**). Scale bar, 100 μm (**A**–**D**). Source data are provided as a Source Data file.

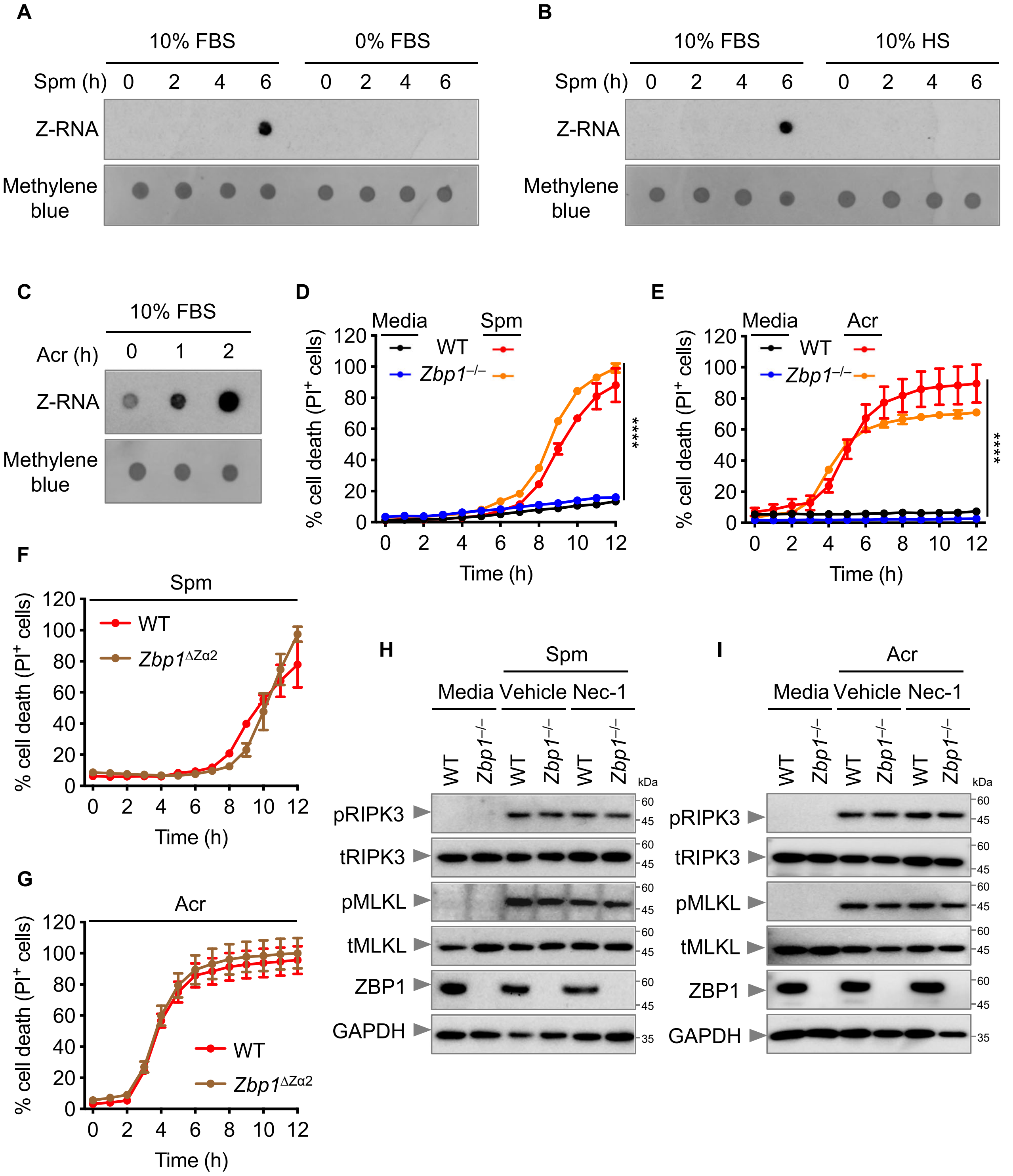

Fig. 4 | Spermine and acrolein induce accumulation of Z-RNA. A–C Dot blot analysis for Z-RNA in bone marrow-derived macrophages (BMDMs) after stimulation with (**A**) spermine (Spm) with or without fetal bovine serum (FBS); (**B**) Spm with FBS or human serum (HS); (**C**) acrolein (Acr) in FBS. **D, E** Real-time analysis of cell death in wild-type (WT) and *Zbp1*$^{-/-}$ BMDMs treated with (**D**) Spm; (**E**) Acr. **F, G** Real-time analysis of cell death in WT and *Zbp1*$^{\Delta Z\alpha 2}$ BMDMs treated with (**F**) Spm; (**G**) Acr. **H, I** Immunoblot analysis of phosphorylated receptor-interacting serine/threonine kinase 3 (pRIPK3), total RIPK3 (tRIPK3), phosphorylated mixed lineage kinase domain-like pseudokinase (pMLKL), and total MLKL (tMLKL) in WT and *Zbp1*$^{-/-}$ BMDMs treated with (**H**) Spm; (**I**) Acr in the presence or absence of necrostatin-1 (Nec-1). GAPDH was used as an internal control. Data are shown as mean ± SEM; ****$P < 0.0001$ (two-way ANOVA and two-tailed *t* test; $n = 4$ from 4 biologically independent samples) (**D**–**G**). Data are representative of at least three independent experiments (**A**–**C**, **H,** and **I**). Source data are provided as a Source Data file.

SAT1-deficient (*Sat1*$^{-/-}$) HeLa cells were treated with TSZ. Notably, *Sat1*$^{-/-}$ HeLa cells exhibited significantly increased cell death compared to WT cells following stimulation with TSZ (Fig. 5H and Supplementary Fig. 9C), suggesting that SAT1 activity inhibits necroptosis. Since chemoproteomic profiling did not identify MLKL as a direct target of acrolein, we hypothesized that acrolein may instead target molecules crucial for MLKL oligomerization and membrane translocation. Supporting this hypothesis, we identified heat shock protein 90 (HSP90)

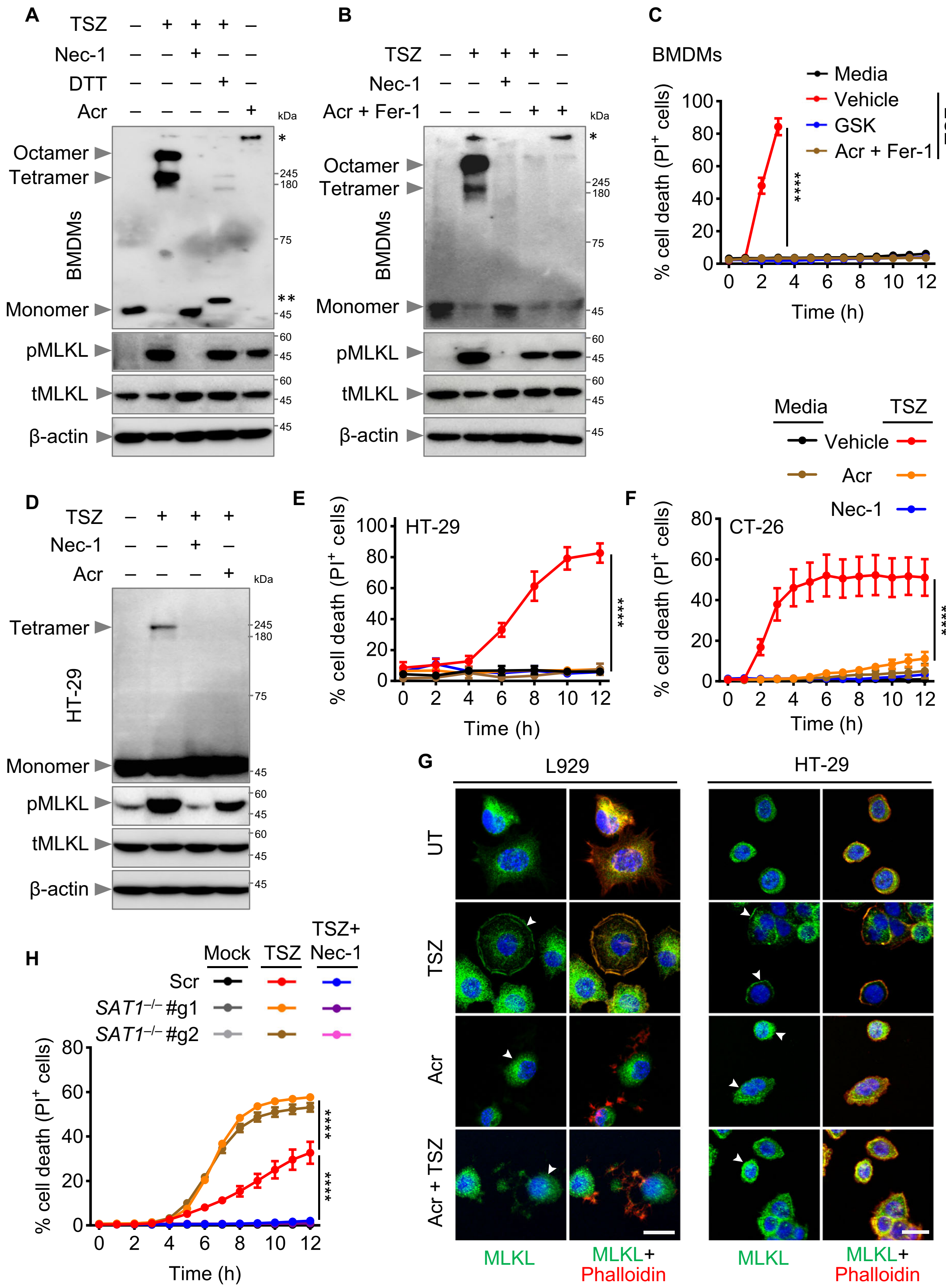

as a target of acrolein (Supplementary Data 1). HSP90 activity is known to be required for the induction of necroptosis by promoting MLKL oligomerization and membrane translocation[62]. Altogether, these data indicate that acrolein, a byproduct of polyamine metabolism, inhibits necroptosis by blocking MLKL oligomerization and membrane translocation.

Acrolein sequestration unleashes necroptosis and improves anti-cancer therapy

Acrolein is produced as a byproduct of necroptosis-triggering chemotherapy agents, such as cyclophosphamide and ifosfamide[63]. We hypothesized that acrolein could result in unintended consequences of lowering efficacy of chemotherapies due to its ability to induce

Fig. 5 | Acrolein hinders necroptosis via targeting MLKL oligomerization. **A**, **B** Immunoblot analysis of mixed lineage kinase domain-like pseudokinase (MLKL) oligomers by detecting total MLKL (tMLKL) in non-reducing condition and immunoblot analysis of phosphorylated MLKL (pMLKL) and tMLKL in bone marrow-derived macrophages (BMDMs) after indicated treatments. The single asterisk (*) indicates the band for potential higher molecular weight aggregates and the double asterisks (**) indicate the band for reduced monomer of MLKL. TSZ [murine TNF, Smac-mimetic and Z-VAD-FMK (zVAD)], necrostatin-1 (Nec-1), dithiothreitol (DTT), acrolein (Acr), and ferrostatin-1 (Fer-1) were used. β-actin was used as an internal control. **C** Real-time analysis of cell death of BMDMs with TSZ as described in the presence of GSK'872 (GSK) or Acr combined with Fer-1. **D** Immunoblot analysis of MLKL oligomers by detecting total MLKL under non-reducing conditions and immunoblot analysis of pMLKL and tMLKL in TSZ (human TNF, Smac-mimetic, and zVAD)-treated HT-29 cells with or without Nec-1 and Acr. **E**, **F** Real-time analysis of cell death in TSZ-treated (**E**) HT-29 cells and (**F**) CT-26 cells with or without Acr and Nec-1. **G** Representative images of MLKL immunofluorescence in TSZ-treated L929 cells and HT-29 cells as described in the presence or absence of Acr. White arrowheads indicate MLKL puncta. **H** Real-time analysis of cell death in RIPK3-expressing HeLa cells exposed to N^1,N^{11}-diethylnorspermine (DENSPM), genetically modified using CRISPR-Cas9 with either a non-targeting scramble guide RNA (Scr) or *SAT1*-specific guide RNAs (*SAT1*$^{-/-}$ #g1 and *SAT1*$^{-/-}$ #g2), treated with TSZ (human TNF, Smac-mimetic BV-6 and zVAD) in the presence or absence of Nec-1. Nec-1, GSK, Fer-1, and Acr were pretreated before TSZ stimulation. BV-6 was used in experiments where specifically noted. Data are representative of at least three independent experiments (**A**, **B**, **D**, and **G**). Data are shown as mean ± SEM; $^{****}P < 0.0001$ (two-way ANOVA; $n = 4$ from 4 biologically independent samples) (**C**, **E**, **F**, and **H**). Scale bar, 20 μm (**G**). Source data are provided as a Source Data file.

---

necroptosis blockade. To test this possibility, CT-26 cells were treated with the preactivated form of cyclophosphamide, 4-hydroperoxycyclophosphamide, and zVAD, which directs cell death towards necroptosis, a process which was blocked by Nec-1 (Fig. 6A). Importantly, the acrolein quencher hydralazine potentiated the death of CT-26 cells induced by 4-hydroperoxycyclophosphamide plus zVAD, which was also inhibited by Nec-1 (Fig. 6A). Altogether, these data suggest that acrolein blocks the cytotoxic effects of cyclophosphamide.

Next, we asked whether the administration of the acrolein quencher hydralazine would improve the anti-cancer efficacy of cyclophosphamide in a physiological setting. CT-26 cells were injected subcutaneously into the flanks of mice. Tumors became palpable 10 days after the injection, at which point drug treatments were initiated. Specifically, administration of cyclophosphamide was found to significantly reduce tumor growth and induce MLKL phosphorylation compared with untreated mice (Fig. 6B, C). Notably, combined administration of cyclophosphamide and hydralazine resulted in a greater attenuation of tumor growth compared with cyclophosphamide treatment alone (Fig. 6B). We also observed a significant expansion of overall necrotic areas and extensive disruption of tissue structures in tumors from mice treated with cyclophosphamide plus hydralazine compared to those treated either with cyclophosphamide or hydralazine alone (Fig. 6C). However, consistent with observations from acrolein-treated cells, phosphorylation of MLKL remained unchanged in tumors from mice treated with cyclophosphamide, with or without hydralazine (Fig. 6C). Notably, the combination of cyclophosphamide plus hydralazine also led to reduced tumor growth in mice injected with human colorectal cancer HT-29 cells (Fig. 6D). These findings suggest that hydralazine enhances the tumor-suppressive effect of cyclophosphamide by potentiating necroptosis in vivo.

Polyamine metabolism and necroptosis associate with increased survival of humans with cancer

To identify links between polyamine metabolism, necroptosis, and cancer prognosis, we analyzed survival data from patients with cancer, stratified by the expression levels of necroptosis-related molecules RIPK3 and MLKL, and enzymes involved in polyamine metabolism. Among 32 cancer types analyzed, we observed significant differences in the overall survival in *RIPK3*$^{\text{High}}$ and *MLKL*$^{\text{High}}$ clusters across kidney renal clear cell carcinoma (KIRC), colon adenocarcinoma (COAD), and lung adenocarcinoma (LUAD). Specifically, KIRC patients with a higher expression of *RIPK3* or *MLKL* showed significantly better prognosis when they were *SAT1*$^{\text{low}}$ compared to *SAT1*$^{\text{High}}$ counterparts (Supplementary Fig. 10A, B). Similarly, a lower expression of amine oxidase copper containing 3 (*AOC3*), an enzyme contributing to polyamine oxidation[64], and spermine oxidase (*SMOX*), an enzyme mediating spermine catabolism[25], correlated with better survival in patients with COAD and LUAD, respectively (Supplementary Fig. 10C–F). Since the lungs, kidneys, and colon are particularly susceptible to acrolein exposure derived from smoking, cyclophosphamide metabolism, and processed food consumption, this analysis highlights the clinical relevance of acrolein exposure in cancer treatment outcomes. Additionally, we explored the role of smoking, a major source of acrolein[65], in cancer therapies through a meta-analysis. Both fixed- and random-effects models revealed that smoking during radiotherapy or chemoradiotherapy significantly increased the overall mortality risk in patients with cancer (Supplementary Fig. 10G). Altogether, we have elucidated a mechanism by which acrolein activates ferroptosis and inhibits necroptosis, and that sequestration of acrolein enhances the efficacy of chemotherapies (Fig. 6E).

Discussion

Cancer cells often develop resistance to chemotherapeutic agents by evading cell death pathways, significantly limiting therapeutic efficacy[14]. While substantial research has focused on the molecular mechanisms conferring chemoresistance, our study highlights a distinct, underexplored phenomenon: ferroptosis-activating metabolites, particularly acrolein, can interfere with the efficacy of chemotherapeutics by inhibiting necroptosis.

In cells cultured with FBS-supplemented media, polyamines such as spermine and spermidine undergo oxidation to produce reactive metabolites including acrolein and H_2O_2. While intracellular H_2O_2 produced during polyamine metabolism can sensitize cells to RSL3-induced ferroptosis[46], our findings demonstrate that H_2O_2 does not mediate ferroptosis induced by polyamines. Notably, exogenous H_2O_2 enhanced RSL3-induced ferroptosis. Therefore, it is possible that H_2O_2 may act as a sensitizing factor, promoting acrolein-induced ferroptosis during polyamine metabolism. Acrolein, in addition to triggering ferroptosis, has been reported to induce other cell death modalities, such as apoptosis and pyroptosis, by activating caspases[66,67]. However, these effects remain to be further validated due to the ability of acrolein to covalently modify and inactivate caspases by adducting to their cysteine residues[68]. In our study, we did not observe activation of any caspases in macrophages treated with acrolein.

SAT1 can sensitize oxidative stress-mediated ferroptosis through arachidonate 15-lipoxgenase (ALOX15) induction[69], but little is known regarding the connection between SAT1 and necroptosis. Our findings demonstrate that SAT1 deletion leads to increased necroptosis, highlighting the contribution of intracellular polyamine metabolism to cell death other than ferroptosis. However, further exploration of other polyamine-catabolizing enzymes, such as SMOX and PAOX, could provide insights into polyamines and necroptosis.

Spermine and spermidine can promote the transition of B-DNA to Z-DNA, suppressing cGAS activity and inhibiting type I IFN production[70]. Consistent with this, we observed spermine induces Z-RNA accumulation, but only in FBS-supplemented media and not in

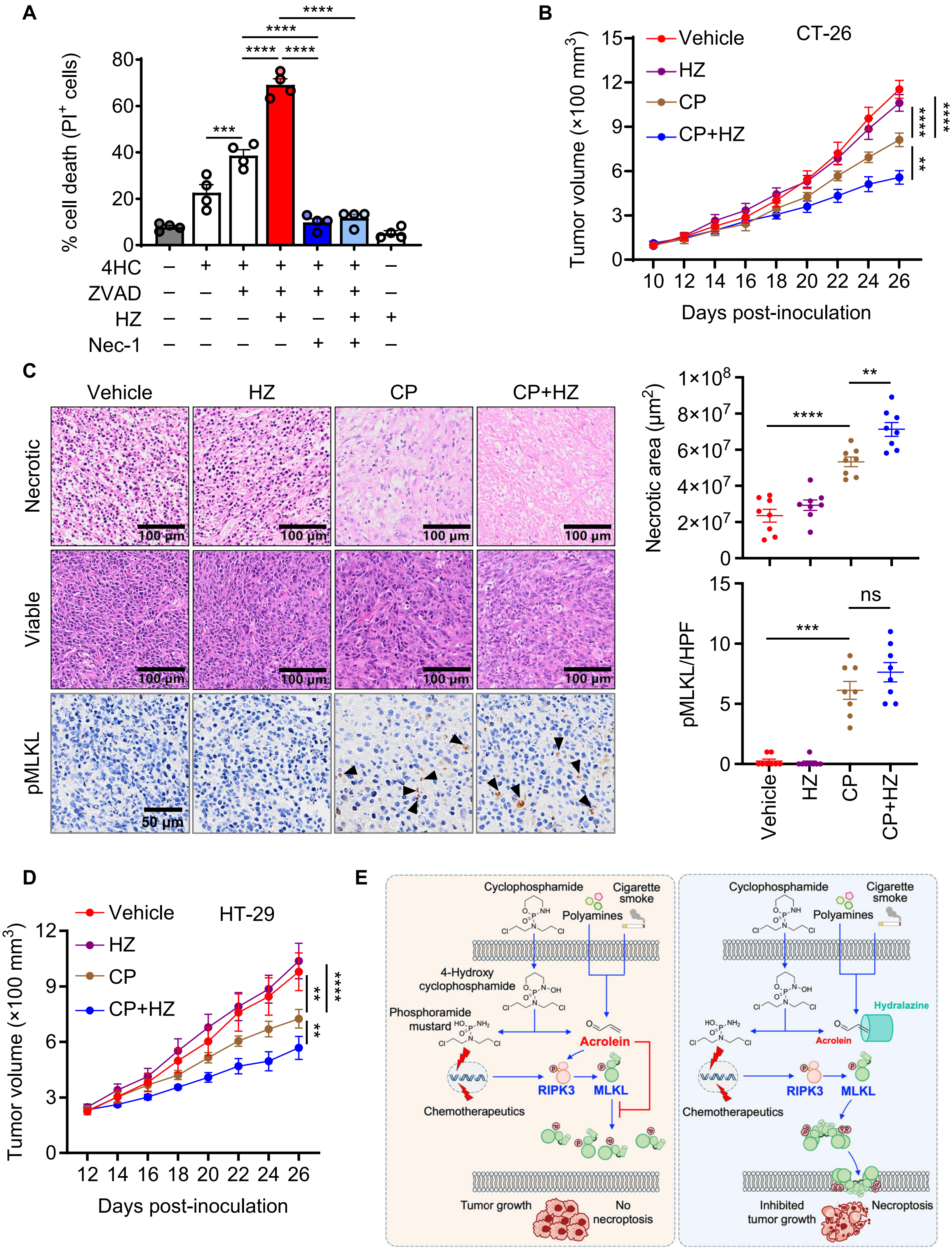

FBS-depleted media or media supplemented with human serum. Importantly, acrolein triggers robust Z-RNA accumulation. Oxidative stress induced by acrolein may trigger Z-RNA accumulation. Since Z-RNAs serve as endogenous ligands for ZBP1, their accumulation under oxidative stress could activate necroptotic signaling pathways[71,72]. Our data demonstrate that neither RIPK1 nor ZBP1 are essential for acrolein-induced phosphorylation of RIPK3 and MLKL. Interestingly, inhibition of ferroptosis prevents cell death without altering acrolein-mediated RIPK3 and MLKL activation.

A key insight from our study is that RIPK3 and MLKL phosphorylation alone does not confirm the execution of necroptosis. Acrolein-induced phosphorylation of these proteins fails to mediate cell death due to impaired MLKL oligomerization. Supporting this finding, necrosulfonamide, a known inhibitor of human MLKL

Fig. 6 | The acrolein scavenger Hydralazine enhances chemotherapeutic efficacy. A Percentage of cell death in CT-26 cells at 48 h after stimulation with one or more of the following: 4-hydroperoxycyclophosphamide (4HC), Z-VAD-FMK (zVAD), hydralazine (HZ), and necrostatin-1 (Nec-1). **B** Mean tumor volume in wild-type (WT) Balb/c mice 10 days after CT-26 cancer cells engraftment, treated with a vehicle, hydralazine (HZ), cyclophosphamide (CP), or CP plus HZ. Mice were treated with CP and/or HZ every 2 days until sacrificed. **C** Representative images of hematoxylin and eosin staining in necrotic (top row) and viable (middle row) tumor regions, immunohistochemical staining of phosphorylated mixed lineage kinase domain-like pseudokinase (pMLKL, bottom row), and quantification of necrotic areas or pMLKL-positive cells per high-power field (HPF). Each dot represents mean necrotic area or pMLKL-positive cells per mouse. **D** Mean tumor volume in WT Balb/c nude mice 12 days after HT-29 cancer cells engraftment, treated with vehicle, HZ, CP, or CP plus HZ. Mice were treated with CP and/or HZ every 2 days until sacrificed. **E** Schematics depicting the mechanisms by which metabolically-derived or exogenously sourced acrolein inhibits necroptosis and promotes chemoresistance. Data are shown as mean ± SEM (**A**–**D**). ****$P < 0.0001$ and ***$P = 0.0005$ (one-way ANOVA; $n = 4$ from 4 biologically independent samples) (**A**). ****$P < 0.0001$ and **$P = 0.0024$ (two-way ANOVA; $n = 10$ per group) (**B**). ****$P < 0.0001$, ***$P = 0.0009$, **$P = 0.0097$ and ns = 0.4714 (one-way ANOVA; $n = 8$) (**C**). ****$P < 0.0001$, **$P = 0.0032$ for vehicle versus CP and **$P = 0.0029$ for CP versus CP plus HZ (two-way ANOVA; for vehicle, $n = 7$ and others, $n = 8$ per group) (**D**). Scale bars, 100 µm for hematoxylin and eosin staining and 50 µm for immunohistochemical staining. Source data are provided as a Source Data file.

oligomerization, blocks necroptosis without interfering with RIPK3 or MLKL phosphorylation[11]. These observations challenge the prevailing assumption that phosphorylation of RIPK3 or MLKL is a definitive marker of necroptosis and underscore the necessity of examining MLKL oligomerization when determining necroptotic activity.

Inducing necroptosis represents a promising strategy to overcome apoptosis resistance in tumors[73]. Our findings reveal that acrolein, a byproduct of polyamine metabolism and chemotherapeutic agents such as cyclophosphamide and ifosfamide[23], inhibits necroptotic signaling by preventing MLKL oligomerization. This inhibition likely contributes to the reduced efficacy of certain chemotherapeutics. Acrolein is also found in cigarette smoke, with concentrations reaching up to 90 ppm[74]. Fluids covering the respiratory tract lining may contain acrolein at concentrations as high as 80 µM[65]. Chronic exposure to acrolein from smoking correlates with increased chemoresistance and poor survival outcomes in patients with lung cancer[75,76]. Additionally, acrolein derived from cyclophosphamide and ifosfamide has been implicated in bladder toxicity[23], potentially via ferroptosis. We demonstrate that trapping acrolein using hydralazine, a vasodilator approved for hypertension[77], restores necroptotic signaling and enhances the anti-cancer efficacy of cyclophosphamide. The dual effects of hydralazine—mitigating acrolein-mediated ferroptosis in urinary bladder and promoting necroptosis of cancer cells—underscore its potential as an adjuvant therapy in cancer treatment.

Overall, our study demonstrates that metabolically generated acrolein impedes necroptosis by inhibiting MLKL oligomerization, thereby undermining the anti-cancer efficacy of cell death-inducing agents. These results advocate for the use of acrolein-trapping agents to enhance therapeutic efficacy by unleashing necroptosis functions. This work underscores the critical interplays between metabolism and cell death, providing a foundation for improving cancer therapies through metabolic intervention.

Methods

The use of animals in this research complies with all relevant ethical regulations of Institutional Animal Care and Use Committee of Seoul National University and Institutional Animal Care and Use Committee of Shenzhen Bay Laboratory.

Mice

Wild-type (WT) C57BL/6J mice were purchased from Raonbio (Yongin, Korea). *Nlrp3*$^{-/-}$, *Aim2*$^{-/-}$, *Nlrc4*$^{-/-}$, *Mefv*$^{-/-}$, *Casp1*$^{-/-}$, *Ifnar1*$^{-/-}$, and *Zbp1*$^{-/-}$ mice were kindly provided by Dr. SangJoon Lee (Ulsan National Institute of Science and Technology)[78]. *Zbp1*$^{\Delta Z\alpha 2}$ mice were kindly received from Dr. Thirumala-Devi Kanneganti (St. Jude Children's Research Hospital)[79]. *Mlkl*$^{-/-}$ mice were kindly provided by Dr. Jaewhan Song (Yeonsei University). Mice were housed and bred under protocols approved by the Seoul National University Institutional Animal Care and Use Committee. Mice were maintained with a 12 h of light/dark cycle under 23–26 °C temperature and 45% humidity and were provided with ad libitum access to water and standard chow (Altromin, 1314). Both male and female, age- and sex-matched, 6- to 9-week old mice were used in this study. For the information on mice used for tumor transplant models, refer to 'in vivo experiments'.

Generation of immortalized BMDMs

Wild-type (WT) primary BMDMs were transformed using established protocols[80]. BMDMs were cultured with J2Cre virus 74 for 48 h, after which L-cell conditioned medium was gradually reduced over a period of 6–10 weeks.

Cell culture

Primary bone marrow-derived macrophages (BMDMs) were obtained from the bone marrow of WT and knockout mice as described previously[81]. Cells were cultured for 7 days in Dulbecco's modified Eagle's medium (DMEM; Biowest, L0103-500) with 30% L929-conditioned media, 10% heat-inactivated fetal bovine serum (FBS; Gibco, 16000044), 1% penicillin and streptomycin (Biowest, L0022-100), and 1% non-essential amino acids (Gibco, 11140-050). BMDMs were then seeded in DMEM media supplemented with 1% non-essential amino acids, 1% penicillin and streptomycin and 10% heat-inactivated FBS, at a density of 3×10^5 cells, into 24-well plates and incubated at 37 °C overnight unless otherwise described. In the indicated experiments, DMEM media supplemented with 10% human serum (Biowest, S4190), 1% penicillin and streptomycin, and 1% non-essential amino acids were used during stimulation procedures. Immortalized BMDMs (iBMDMs) were grown in DMEM supplemented with 10% BMDM media, 10% FBS, 1% penicillin and streptomycin, and 1% non-essential amino acids. The murine metastatic colon cancer cell line CT-26 (KCLB, 80009) was cultured in DMEM media supplemented with 1% non-essential amino acids, 1% penicillin and streptomycin and 10% heat-inactivated FBS, seeded at 2×10^5 cells into 24-well plates and incubated overnight. The human colon cancer cell line HT-29 (KCLB, 30038) was cultured in RPMI media (Biowest, L0498-500) supplemented with 10% heat-inactivated FBS, 1% penicillin and streptomycin, 1% non-essential amino acids, and 25 mM HEPES (Biowest, L0180-100), seeded at 2×10^5 cells into 24-well plates and incubated overnight. The human lung cancer cell line A549 (KCLB, 10185) was cultured in RPMI media supplemented with 10% heat-inactivated FBS, 1% penicillin and streptomycin, 1% non-essential amino acids, and 25 mM HEPES. The human renal cancer cell lines A498 (KCLB, 30044) and Caki-1 (KCLB, 30046) were cultured in DMEM media supplemented with 1% non-essential amino acids, 1% penicillin and streptomycin, and 10% heat-inactivated FBS. The murine fibroblast cell line L929 (ATCC, CCL-1) was cultured in Iscove's modified Dulbecco's medium (IMDM; Thermo Fischer Scientific, 12440053) supplemented with 10% FBS, 1% penicillin and streptomycin, and 1% non-essential amino acid. The human cervical cancer cell line HeLa (ATCC, CCL-2) was cultured in minimum essential medium Eagle (Sigma, M0643) supplemented with 1% penicillin and streptomycin, and 10% heat-inactivated FBS.

Cell stimulation

Seeded cells were gently washed with PBS before stimulation. Cells were treated with 50 µM spermine (Sigma, S4264), 100 µM spermidine (Sigma, S0266), and 100 µM acrolein (Restek, 30646) unless otherwise noted. Putrescine dihydrochloride (Sigma, P5780) and L-ornithine monohydrochloride (Sigma, O6503) were used at the indicated doses. Unless otherwise noted, the following were used: 100 ng/mL recombinant murine TNF (Peprotech, 315-1 A), 100 ng/mL recombinant human TNF (Peprotech, 300-01 A), 200 nM Smac mimetic LCL161 (Selleckchem, S7009), 5 µM Smac mimetic BV-6 (Selleckchem, S7597), 25 µM Z-VAD-FMK (Selleckchem, S7023), 20 µM necrostatin-1 (Selleckchem, S8037), 5 µM ras-selective lethal molecule 3 (RSL3; Selleckchem, S8155), 10 µM ferrostatin-1 (Sigma, SML0583), corresponding doses of dimethyl sulfoxide (Sigma, D2650), 10 µM GSK'872 (Selleckchem, S8465), 2.5 mM 1,4-dithiothreitol (DTT; Roche, 10708984001), 10 µM N^1,N^{11}-diethylnorspermine tetrahydrochloride (DENSPM; MCE, HY-13610A), 5 µM 4-hydroperoxycyclophosphamide (Cayman, 19527), 100 µM hydralazine hydrochloride (Sigma, H1753), 10 mM sodium pyruvate (Biowest, L0642), and 20 µM deferoxamine mesylate (Selleckchem, S5742).

Generation of knockout cells

To generate HeLa cells constitutively expressing RIPK3, *RIPK3* was inserted into the vector lentiCas9-Blast (Addgene, 52962) by replacing the Cas9 gene. The plasmid carrying *RIPK3* was co-transfected with the packaging plasmids psPAX2 and pMD2.G into HEK293T cells. Lentiviruses were harvested twice at days 2 and 3 post-transfection. HeLa cells were transduced with the harvested lentivirus in the presence of polybrene (Sigma, 107689), and selected with blasticidin for at least one week. The expression of RIPK3 in the newly generated HeLa-RIPK3 cell line was confirmed by immunoblotting. This cell line was maintained in DMEM supplemented with 10% FBS. HeLa-RIPK3-SAT1 knockout (KO) cell lines were then generated using CRISPR-Cas9 technology. Two sgRNAs targeting *SAT1* (sgRNA #g1 5′-GCTGGCTAAATATGAATACA-3′, #g2 5′-CAAGTAATCTTAACTGAAAA-3′) were cloned into the pX458 vector. HeLa-RIPK3 cells were transfected with pX458-SAT1 sgRNA plasmids using Lipo8000™ (Beyotime Biotechnology). GFP-positive cells were sorted using a flow cytometer, and single-cell clones were selected. To validate $SAT1^{-/-}$ cells, the clones were treated with DENSPM to induce SAT1 expression. Positive clones lacking SAT1 protein expression were identified using immunoblotting.

Lipid peroxidation quantification

Boron dipyrromethane difluoride (BODIPY)-C11 is a fluorescent reporter dye that is widely used to measure oxidized phospholipids as a marker of intracellular lipid peroxides[82]. Cells were stained with 5 µM $BODIPY^{581/591}$-C11 dye (Invitrogen, D3861) at the time of stimulation with the indicated reagents. Fluorescence of $BODIPY^{581/591}$-C11 was measured by simultaneous acquisition of the green and red signals using the IncuCyte SX5 (Sartorius) live-cell automated system. The red fluorescence corresponds to the non-oxidized fraction and the green fluorescence corresponds to the oxidized fraction of the probe. The oxidation ratio was calculated as an indicator of lipid peroxidation.

Real-time imaging for cell death

The kinetics of cell death were quantified using the IncuCyte SX5 (Sartorius) live-cell automated system. Primary BMDMs, iBMDMs, L929, CT-26, HT-29, Caki-1, A549, and A498 cells were seeded in 24-well cell culture plates. Cells were treated with the indicated reagents, and stained with propidium iodide (PI; Invitrogen, P3566) or SYTOX™ Green Nucleic Acid Stain (Invitrogen, S7020) according to the manufacturer's protocol. The plates were scanned, and fluorescent and phase-contrast images were acquired in real-time every 1 h from 0 h post-treatment at 37 °C and 5% CO_2. PI- or SYTOX-positive cells were marked with a red mask for visualization. The image analysis, masking, and quantification of PI- or SYTOX-positive cells (dead cells) and cell confluency (%) were performed using the software package supplied with the IncuCyte live-cell automated system. For both BMDMs (differentiated cells) and cancer lines (which undergo further proliferation), cell death was normalized to the percentage confluency data provided by the IncuCyte SX5 software at the real-time point, in order to reflect actual cell numbers. Cell death percentage was yielded using the following calculation:

% cell death = (PI^+ cell count)/[(t_h confluency/0_h confluency) × (seeded cell number)] × 100

t_h confluency: confluency at each time point; 0_h confluency: confluency at 0 h.

Immunoblot analysis

Immunoblotting was performed as described previously[83]. In brief, for the analysis of signaling components, cell culture supernatants were removed, cells were washed once with PBS followed by lysis in RIPA buffer and 4× sample loading buffer (containing SDS and 2-mercaptoethanol). For caspase analysis, cell lysates and supernatants were lysed in caspase lysis buffer (containing 1× protease inhibitors, 1× phosphatase inhibitors, 10% NP-40, and 25 mM DTT)[84]. For the analysis of LDH and HMGB1, cell supernatants were collected and centrifuged at 6000 × *g* for 4 min. Supernatants were carefully collected, and 4× sample loading buffer was added. Proteins were separated in 8–12% polyacrylamide gels using electrophoresis. Proteins were electrophoretically transferred onto PVDF membranes (Millipore, IPVH00010) followed by blocking in TBST with 5% skim milk (CELLNEST, CNS109-0500). Then, membranes were incubated overnight in 4 °C with primary antibodies: anti-GSDMD (abcam, ab209845, 1:1000), anti-GSDME (abcam, ab215191, 1:1000), anti-caspase-1 (Adipogen, AG-20B-0042-C100, 1:1000), anti-caspase-3 (Cell Signaling, 9662S, 1:1000), anti-cleaved caspase-3 (Cell Signaling, 9661S, 1:1000), anti-caspase-7 (Cell Signaling, 9492S, 1:1000), anti-cleaved caspase-7 (Cell Signaling, 9491S, 1:1000), anti-caspase-8 (AdipoGen, AG-20T-0137-C100, 1:1000), anti-RIP3 (Cell Signaling, 95702S, 1:1000), anti-phospho-RIP3 (Cell Signaling, 91702S, 1:1000), anti-MLKL (AdipoGen, AP14272B, 1:1000), anti-phospho-MLKL (Cell Signaling, 37333S, 1:1000), anti-phospho-MLKL Ser358 D6H3V (Cell Signaling, 91689S, 1:1000), anti-MLKL E7V4W (Cell Signaling, 26539S, 1:1000), anti-ZBP1 (AdipoGen, AG-20B-0010-C100, 1:1000), anti-LDHA-specific rabbit polyclonal (Proteintech, 19987-1-AP, 1:1000), anti-HMGB1 (abcam, ab18256, 1:1000), anti-GAPDH (Cell Signaling, 5174S, 1:1000), anti-β-actin (Cell Signaling, 8457S, 1:1000), anti-GPX4 (Abclonal, A1933, 1:1000), anti-thioredoxin 1 (Cell Signaling, C63C6, 1:1000) and anti-SAT1 (Proteintech, 10708-1-AP, 1:1000). Membranes were then washed with TBST and incubated with horseradish peroxidase (HRP)-conjugated secondary antibodies: anti-rabbit (Invitrogen, 31460, 1:5000) or anti-mouse (CELLNEST, CNG004-0005, 1:5000). Protein bands were detected using Immobilon Forte Western HRP Substrate (Millipore, WBLUF0500), and membranes were developed with Amersham ImageQuant 800.

Hydrogen peroxide quantification

BMDM cells were seeded in 12-well plates and stimulated as described above. The culture supernatants were then collected and hydrogen peroxide levels were quantified using Amplex™ Red Hydrogen Peroxide/Peroxidase Assay Kit (Invitrogen, A22188) following the manufacturer's protocol. Samples were prepared in a 96-well black/clear bottom plate and incubated for 30 min. Fluorescence was sequentially measured using Tristar5 multimode microplate reader (BERTHOLD).

RNA dot blot analysis

Dotblotting was performed as described previously[53]. For the extraction of RNAs from cells, culture supernatants were removed and total RNAs were extracted using TRIzol reagent (GLPBIO, GK20008). The isolated RNAs were diluted in RNase-free water to a final concentration of 500 ng/μL as determined by a NanoDrop UV/VIS Spectrophotometer. 1 μg of RNA samples were dotted onto the nylon membrane (Hybond®-N+ hybridization membranes; Cytiva, RPN203B), dried and auto-crosslinked by UV light. The membranes were then stained with methylene blue buffer (0.4 M acetic acid, 0.4 M sodium acetate) for 10 s, followed by 5 times of washing in RNase-free water before colorimetric capture. After washing, membranes were blocked in 5% skim milk in TBST and incubated with an anti-Z-RNA antibody (Absolute antibody, Ab00783-23.0, 1:500) overnight at 4 °C. After rinsing with TBST, membranes were incubated with horseradish peroxidase (HRP)-conjugated secondary antibodies and developed using Immobilon Forte Western HRP Substrate and Amersham ImageQuant 800.

Chemoproteomic profiling

BMDMs were seeded at a density of 5×10^6 cells per 100 mm dish and incubated overnight. Cells were stimulated with 100 μM acrolein for 1 h ($n = 1$). Cells were washed and lysed as described previously[74]. Each sample was reduced with dithiothreitol (Sigma, 43815) at a final concentration of 10 mM and incubated for 30 min at 37 °C. Iodoacetamide (Sigma, I1149) was added at a final concentration of 25 mM for alkylation and incubated for 30 min in the dark at room temperature. After adding 100 mM ammonium bicarbonate (Sigma, A6141) to lower the concentration of urea, trypsin (Promega, V5280) was added at a protein ratio of 1:25 (w/w). Peptide samples were incubated at 37 °C for 16 h and purified with a SOLA HRP 96 well plate C18 cartridge (Thermo Fisher Scientific, 60509-001). The solute was dried and stored at −80 °C. Peptides were reconstituted in 0.1% trifluoroacetic acid (Thermo Fisher Scientific, 28904) and analyzed using Orbitrap Exploris 480 (Thermo Fisher Scientific) coupled with Ultimate 3000 UPLC (Thermo Fisher Scientific). In 200 min of analysis, the flow rate was set to 0.25 μL/min, and the linear gradient of buffer B was set as followed: 2% at 0 min, 2% at 5 min, 10% at 6 min, 30% at 135 min, 54% at 155 min, 95% at 157 min, 95% at 180 min, 95% at 180 min and 2% at 200 min. The mobile phase was prepared in buffer A using 0.1% formic acid (FA; Thermo Fisher Scientific, 28905) in 5% DMSO, and buffer B using 0.1% FA, 5% DMSO in 80% acetonitrile (JTB, 9017-03). Trap column (2 μm, 2 cm × 75 μm, Thermo Fisher Scientific, 164750-CCS) and analytical column (2 μm, 75 μm × 500 mm, Thermo Fisher Scientific, ES903) were used to separate the peptides. Each sample was analyzed using the data-dependent acquisition (DDA) scan method. Resolution was set to 60,000 for MS1 and 30,000 for MS2. Scan range was set to 350–1800 m/z. The Normalized Collision Energy was set to 32% and dynamic exclusion was set to 30 s. The LC-MS/MS raw files were processed using the Sequest HT search engine. The mouse database was downloaded from Uniprot (Mus Musculus, UP000000589). Database search was conducted using Proteome Discoverer (version 2.4) and conditions were limited to peptides having a length of 7 to 50 amino acids, and missed cleavage was allowed up to two. Carbamidomethylation (+ 57.0214 Da, C) and oxidation (+ 15.9949 Da, M) were considered as peptide modifications. In addition, acrolein 38 (+ 38.016 Da), acrolein 56 (+ 56.026 Da), acrolein 58 (+ 58.042 Da) and acrolein 112 (+ 112.052 Da) were considered for cysteine, histidine, lysine and arginine. False discovery rate (FDR) was applied at 1% each at the spectrum, peptide, and protein levels. To identify ferroptosis-related molecules potentially modified by acrolein, we utilized datasets of drivers, markers, and suppressors from the Ferroptosis Database (FerrDb V2, http://www.zhounan.org/ferrdb/current/). These datasets were compared with the modified adducts identified in mass spectrometry to determine overlapping genes encoding the corresponding proteins.

Non-reducing SDS-PAGE

For the analysis of MLKL oligomerization using non-reducing SDS-PAGE, culture supernatants were removed, followed by lysis in RIPA buffer and dispensed into two aliquots of equal volume. One set of lysates were mixed with non-reducing 4× loading dye (0.5% TAE buffer, 20% glycerol, 8% Sarkosyl, 0.1 mg/ml bromophenol blue, 1× protease inhibitors, 1× phosphatase inhibitors added) to preserve disulfide bonds. Another set was prepared for regular immunoblotting procedure as described. Non-reduced protein samples were run at a constant 80 V in 10% polyacrylamide gel until protein monomers migrated to the bottom of the gel. Further processes followed immunoblotting procedure as described. Paired immunoblotting was performed following immunoblotting protocol described above.

Immunofluorescence staining

L929 and HT-29 cells were seeded onto 8-chamber slides at densities of 4×10^4 and 1×10^5 cells per well, respectively, and incubated overnight. After stimulation, cells were gently washed with PBS. Samples were fixed with 4% paraformaldehyde in PBS for 15 min at room temperature, followed by three PBS washes. For blocking and permeabilization, cells were incubated in 1% BSA solution in PBS containing 0.3% Triton X-100 (Sigma, T8787) for 1 h at room temperature. Subsequently, cells were incubated overnight at 4 °C with an anti-MLKL antibody (E7V4W, Cell Signaling, 26539S, 1:200) diluted in 1% BSA solution in PBS with 0.3% Triton X-100. The slides were washed three times with PBS and then incubated with Alexa Fluor® 488 AffiniPure™ F(ab')$_2$ Fragment Donkey Anti-Mouse IgG (H + L) (Jackson ImmunoResearch, 715-546-150, 1:1000) for 1 h at room temperature. After five PBS washes, cells were counterstained with DAPI (Invitrogen, D1306) and Alexa Fluor™ 568 Phalloidin (Invitrogen, A12380) in 1% BSA solution in PBS with 0.3% Triton X-100 for 30 min at room temperature. Following four PBS washes and a final wash with distilled water, samples were mounted using Immu-Mount (epredia, 9990402). Visualization was performed using an LSM 700 system (Carl Zeiss), and images were captured with ZEISS ZEN 3.11 software.

In vivo experiments

The use of mouse tumor transplant models in this research complies with all relevant ethical regulations of Institutional Animal Care and Use Committee of Shenzhen Bay Laboratory. Male and female Balb/c mice or Balb/c nude mice (7–8 weeks old) were purchased from Vital River Laboratory Animal Technology (Beijing, China) and Shanghai Model Organisms Center, Inc. (Shanghai, China), respectively. All mice were maintained under specific pathogen-free conditions at the Institute of Infectious Diseases, Shenzhen Bay Laboratory, China. Mice were maintained with a 12 h of light/dark cycle under 24–26 °C temperature and 50% humidity and were provided with ad libitum access to water and standard chow (LabDiet, 5053). For the syngeneic tumor model, CT-26 or HT-29 cells were suspended in 100 μL of PBS and then subcutaneously injected into the right flank of Balb/c mice or Balb/c nude mice at concentrations of 5×10^5 or 2×10^5 cells per mouse, respectively. On day 10 for Balb/c and day 12 for Balb/c nude mice post-inoculation, mice received intraperitoneal injections of 50 mg/kg cyclophosphamide (Sigma, PHR1404), 5 mg/kg hydralazine (Sigma, H1753), or a combination of both every two days. PBS was used as the vehicle control. Tumor volume (mm^2) was measured on specified days after inoculation and calculated using the formula: [length × width^2 × 0.5]. To evaluate the late-stage necrotic areas in CT-26 tumors, the entire tumor mass was excised from each group and fixed in 4% buffered formalin. Fixed tumors were embedded and subjected to hematoxylin and eosin staining as well as immunostaining for phosphorylated MLKL (pMLKL) using standard histological procedures. Images were captured using the Olympus SLIDEVIEW VS200 system. Necrotic areas were quantified using OLYMPUS OlyVIA 4.1 software and pMLKL-positive cells were counted per high-power field (HPF). The maximal tumor burden permitted by the ethics committee is a volume of 1500 mm^3, and the maximal tumor burden did not exceed the limit.

Survival analysis

RNA-seq data were obtained from The Cancer Genome Atlas (TCGA) (https://www.cancer.gov/tcga) and processed using the TCGA biolinks R package (v2.22.3). The RNA-seq data from 32 primary solid tumor (TP) cancers, encompassing over 9000 tumor samples were included in our analysis. Gene symbols were converted to official HUGO Gene Nomenclature Committee (HGNC) gene symbols, and genes without valid symbols or gene annotations were excluded, yielding 23,216 genes for downstream analyses. For each cancer type, samples were quantile normalized using preprocessCore (v1.56.0) and log2 transformed for further analysis. Gene set enrichment scores representing pathway activities were calculated using the GSVA R package (v1.52.2)[85]. The quantile-normalized, log2-transformed RNA-seq matrices for each cancer type, along with genes encoding MLKL and RIPK3, and genes encoding molecules of polyamine metabolism, such as SAT1, SMOX, and AOC3, were used for further analysis. Samples were stratified into two groups for each gene within a cancer type, using the mean gene expression as the threshold. Samples with expression scores ≥ the mean were designated as “High”, whereas those with scores <the mean were labeled as “Low”. Overall survival (OS) data from the TCGA clinical resource were used to construct Kaplan–Meier survival curves. Patients with <1 day of follow-up were excluded, and survival data were censored at a maximum follow-up duration of 10 years. For each cancer type, samples were classified into *RIPK3*$^{\mathrm{High}}$ and *RIPK3*$^{\mathrm{Low}}$ groups based on mean *RIPK3* expression. Similarly, samples were categorized into *MLKL*$^{\mathrm{High}}$ and *MLKL*$^{\mathrm{Low}}$ groups using the mean *MLKL* expression. Each necroptosis gene expression group (e.g., *RIPK3*$^{\mathrm{High}}$ or *MLKL*$^{\mathrm{High}}$) was further stratified into High and Low sub-clusters for polyamine metabolism genes, based on mean expression of genes encoding SAT1, AOC3, or SMOX. Survival differences between sub-clusters (e.g., *SAT1*$^{\mathrm{High}}$ vs. *SAT1*$^{\mathrm{Low}}$, *AOC3*$^{\mathrm{High}}$ vs. *AOC3*$^{\mathrm{Low}}$, *SMOX*$^{\mathrm{High}}$ vs. *SMOX*$^{\mathrm{Low}}$) were evaluated within each necroptosis gene cluster for all cancer types using the ‘analyze_survival’ and ‘kaplan_meier_plot’ functions from the survivalAnalysis R package. Univariate survival analyses were conducted, and significant differences ($P < 0.1$) were visualized in Kaplan–Meier plots.

Meta-analysis of relative risk estimation

Seven studies[86–92] were included in our meta-analysis to evaluate the effects of smoking during radiotherapy or chemoradiotherapy on the overall mortality risk in cancer patients. The meta-analysis was conducted using the ‘metabin’ and ‘forest’ functions from the meta package (Schwarzer 2007, version 7.0-0) in R 4.2.1. Both fixed- and random-effects models were employed to estimate the pooled relative risk (RR) of mortality associated with smoking and alcohol consumption during radiotherapy. The fixed-effects model, utilizing the Mantel-Haenszel method, assumes a consistent true effect size across all studies. In contrast, the random-effects model, based on the inverse-variance method, accounts for heterogeneity between studies (Schwarzer 2007, version 7.0-0). A forest plot was generated to visualize the relative risk estimates, along with confidence intervals for each study and the overall pooled estimate derived from both the fixed- and random-effects models.

Quantification and statistical analysis

GraphPad Prism 10.2.3 software was used for data analysis. Data are shown as mean ± SEM. Statistical significance was determined by two-tailed t tests for two groups or one-way ANOVA or two-way ANOVA (with Tukey’s multiple comparisons test) for three or more groups. P values less than 0.05 were considered statistically significant where $^{*}P < 0.05$, $^{**}P < 0.01$, $^{***}P < 0.001$, and $^{****}P < 0.0001$.

Reporting summary

Further information on research design is available in the Nature Portfolio Reporting Summary linked to this article.

Data availability

The mass spectrometry proteomics data generated in this study have been deposited in the ProteomeXchange Consortium via the PRIDE partner repository under accession code PXD059944. The Uniprot *Mus Musculus* UP000000589 data and Ferroptosis Database (FerrDb V2) used in this study are available at [https://www.uniprot.org/proteomes/UP000000589] and [http://www.zhounan.org/ferrdb/current/]. The publicly available TCGA data are available at [https://www.cancer.gov/tcga]. The remaining data are available within the Article, Supplementary Information or Source Data file. Source data are provided with this paper. Correspondence and requests for materials should be addressed to R.K. Source data are provided with this paper.

References

1. Newton, K., Strasser, A., Kayagaki, N. & Dixit, V. M. Cell death. *Cell* **187**, 235–256 (2024).
2. Lee, E., Song, C. H., Bae, S. J., Ha, K. T. & Karki, R. Regulated cell death pathways and their roles in homeostasis, infection, inflammation, and tumorigenesis. *Exp. Mol. Med.* **55**, 1632–1643 (2023).
3. Man, S. M. & Kanneganti, T. D. Innate immune sensing of cell death in disease and therapeutics. *Nat. Cell Biol.* **26**, 1420–1433 (2024).
4. Shi, J. et al. Cleavage of GSDMD by inflammatory caspases determines pyroptotic cell death. *Nature* **526**, 660–665 (2015).
5. Rogers, C. et al. Cleavage of DFNA5 by caspase-3 during apoptosis mediates progression to secondary necrotic/pyroptotic cell death. *Nat. Commun.* **8**, 14128 (2017).
6. Li, P. et al. Cytochrome c and dATP-dependent formation of Apaf-1/caspase-9 complex initiates an apoptotic protease cascade. *Cell* **91**, 479–489 (1997).
7. Muzio, M., Salvesen, G. S. & Dixit, V. M. FLICE induced apoptosis in a cell-free system. Cleavage of caspase zymogens. *J. Biol. Chem.* **272**, 2952–2956 (1997).
8. Slee, E. A., Adrain, C. & Martin, S. J. Executioner caspase-3, −6, and −7 perform distinct, non-redundant roles during the demolition phase of apoptosis. *J. Biol. Chem.* **276**, 7320–7326 (2001).
9. Degterev, A. et al. Identification of RIP1 kinase as a specific cellular target of necrostatins. *Nat. Chem. Biol.* **4**, 313–321 (2008).
10. Degterev, A. et al. Chemical inhibitor of nonapoptotic cell death with therapeutic potential for ischemic brain injury. *Nat. Chem. Biol.* **1**, 112–119 (2005).
11. Sun, L. et al. Mixed lineage kinase domain-like protein mediates necrosis signaling downstream of RIP3 kinase. *Cell* **148**, 213–227 (2012).
12. Dixon, S. J. et al. Ferroptosis: an iron-dependent form of nonapoptotic cell death. *Cell* **149**, 1060–1072 (2012).
13. Strasser, A. & Vaux, D. L. Cell death in the origin and treatment of cancer. *Mol. Cell* **78**, 1045–1054 (2020).
14. Hanggi, K. & Ruffell, B. Cell death, therapeutics, and the immune response in cancer. *Trends Cancer* **9**, 381–396 (2023).
15. Karki, R., Man, S. M. & Kanneganti, T. D. Inflammasomes and cancer. *Cancer Immunol. Res.* **5**, 94–99 (2017).
16. Hanahan, D. & Weinberg, R. A. The hallmarks of cancer. *Cell* **100**, 57–70 (2000).
17. Mansoori, B., Mohammadi, A., Davudian, S., Shirjang, S. & Baradaran, B. The different mechanisms of cancer drug resistance: a brief review. *Adv. Pharm. Bull.* **7**, 339–348 (2017).
18. Zang, X., Song, J., Li, Y. & Han, Y. Targeting necroptosis as an alternative strategy in tumor treatment: From drugs to nanoparticles. *J. Control Release* **349**, 213–226 (2022).
19. Gong, Y. et al. The role of necroptosis in cancer biology and therapy. *Mol. Cancer* **18**, 100 (2019).
20. Pathania, S., Bhatia, R., Baldi, A., Singh, R. & Rawal, R. K. Drug metabolizing enzymes and their inhibitors’ role in cancer resistance. *Biomed. Pharmacother.* **105**, 53–65 (2018).

21. Michael, M. & Doherty, M. M. Tumoral drug metabolism: overview and its implications for cancer therapy. *J. Clin. Oncol.* **23**, 205–229 (2005).
22. Verma, H., Singh Bahia, M., Choudhary, S., Kumar Singh, P. & Silakari, O. Drug metabolizing enzymes-associated chemo resistance and strategies to overcome it. *Drug Metab. Rev.* **51**, 196–223 (2019).
23. Brock, N. The development of mesna for the inhibition of urotoxic side effects of cyclophosphamide, ifosfamide, and other oxazaphosphorine cytostatics. *Recent Results Cancer Res.* **74**, 270–278 (1980).
24. Casero, R. A. Jr., Murray Stewart, T. & Pegg, A. E. Polyamine metabolism and cancer: treatments, challenges and opportunities. *Nat. Rev. Cancer* **18**, 681–695 (2018).
25. Casero, R. A. & Pegg, A. E. Polyamine catabolism and disease. *Biochem. J.* **421**, 323–338 (2009).
26. Pegg, A. E. Toxicity of polyamines and their metabolic products. *Chem. Res. Toxicol.* **26**, 1782–1800 (2013).
27. Babbar, N. & Casero, R. A. Jr. Tumor necrosis factor-alpha increases reactive oxygen species by inducing spermine oxidase in human lung epithelial cells: a potential mechanism for inflammation-induced carcinogenesis. *Cancer Res.* **66**, 11125–11130 (2006).
28. Sierra, J. C. et al. Spermine oxidase mediates Helicobacter pylori-induced gastric inflammation, DNA damage, and carcinogenic signaling. *Oncogene* **39**, 4465–4474 (2020).
29. Wu, D. et al. Regulation of spermine oxidase through hypoxia-inducible factor-1alpha signaling in retinal glial cells under hypoxic conditions. *Invest. Ophthalmol. Vis. Sci.* **61**, 52 (2020).
30. Chan, F. K., Moriwaki, K. & De Rosa, M. J. Detection of necrosis by release of lactate dehydrogenase activity. *Methods Mol. Biol.* **979**, 65–70 (2013).
31. Scaffidi, P., Misteli, T. & Bianchi, M. E. Release of chromatin protein HMGB1 by necrotic cells triggers inflammation. *Nature* **418**, 191–195 (2002).
32. Bergsbaken, T., Fink, S. L. & Cookson, B. T. Pyroptosis: host cell death and inflammation. *Nat. Rev. Microbiol.* **7**, 99–109 (2009).
33. Fink, S. L. & Cookson, B. T. Caspase-1-dependent pore formation during pyroptosis leads to osmotic lysis of infected host macrophages. *Cell Microbiol.* **8**, 1812–1825 (2006).
34. Galluzzi, L. & Kroemer, G. Necroptosis: a specialized pathway of programmed necrosis. *Cell* **135**, 1161–1163 (2008).
35. Khokhar, S. & Chawla, R. Apoptosis: an ocular perspective. *Natl. Med. J. India* **15**, 148–153 (2002).
36. Man, S. M., Karki, R. & Kanneganti, T. D. Molecular mechanisms and functions of pyroptosis, inflammatory caspases and inflammasomes in infectious diseases. *Immunol. Rev.* **277**, 61–75 (2017).
37. Yuk, H., Abdullah, M., Kim, D. H., Lee, H. & Lee, S. J. Necrostatin-1 prevents ferroptosis in a RIPK1- and IDO-independent manner in hepatocellular carcinoma. *Antioxidants (Basel)* **10**, 1347 (2021).
38. Aleem, A. M. et al. Ferroptosis Inhibitors suppress prostaglandin synthesis in lipopolysaccharide-stimulated macrophages. *ACS Chem. Biol.* **18**, 404–418 (2023).
39. Yang, W. S. et al. Regulation of ferroptotic cancer cell death by GPX4. *Cell* **156**, 317–331 (2014).
40. Wu, J. et al. Intercellular interaction dictates cancer cell ferroptosis via NF2-YAP signalling. *Nature* **572**, 402–406 (2019).
41. Murray Stewart, T., Dunston, T. T., Woster, P. M. & Casero, R. A. Jr. Polyamine catabolism and oxidative damage. *J. Biol. Chem.* **293**, 18736–18745 (2018).
42. Averill-Bates, D. A., Agostinelli, E., Przybytkowski, E., Mateescu, M. A. & Mondovi, B. Cytotoxicity and kinetic analysis of purified bovine serum amine oxidase in the presence of spermine in Chinese hamster ovary cells. *Arch. Biochem. Biophys.* **300**, 75–79 (1993).
43. Burcham, P. C., Kerr, P. G. & Fontaine, F. The antihypertensive hydralazine is an efficient scavenger of acrolein. *Redox Rep.* **5**, 47–49 (2000).
44. Hamann, K., Nehrt, G., Ouyang, H., Duerstock, B. & Shi, R. Hydralazine inhibits compression and acrolein-mediated injuries in ex vivo spinal cord. *J. Neurochem.* **104**, 708–718 (2008).
45. Jackson, J. H., White, C. W., Parker, N. B., Ryan, J. W. & Repine, J. E. Dimethylthiourea consumption reflects H2O2 concentrations and severity of acute lung injury. *J. Appl Physiol. (1985)* **59**, 1995–1998 (1985).
46. Bi, G. et al. Polyamine-mediated ferroptosis amplification acts as a targetable vulnerability in cancer. *Nat. Commun.* **15**, 2461 (2024).
47. Wang, L. et al. Oxidative degradation of polyamines by serum supplement causes cytotoxicity on cultured cells. *Sci. Rep.* **8**, 10384 (2018).
48. Yang, T. et al. Triggering endogenous Z-RNA sensing for anti-tumor therapy through ZBP1-dependent necroptosis. *Cell Rep.* **42**, 113377 (2023).
49. Szczerba, M. et al. Canonical cellular stress granules are required for arsenite-induced necroptosis mediated by Z-DNA-binding protein 1. *Sci. Signal* **16**, eabq0837 (2023).
50. Avezov, K., Reznick, A. Z. & Aizenbud, D. Oxidative damage in keratinocytes exposed to cigarette smoke and aldehydes. *Toxicol. Vitr.* **28**, 485–491 (2014).
51. Jiao, H. et al. Z-nucleic-acid sensing triggers ZBP1-dependent necroptosis and inflammation. *Nature* **580**, 391–395 (2020).
52. Karki, R. et al. ZBP1-dependent inflammatory cell death, PANoptosis, and cytokine storm disrupt IFN therapeutic efficacy during coronavirus infection. *Sci. Immunol.* **7**, eabo6294 (2022).
53. Karki, R. et al. ADAR1 restricts ZBP1-mediated immune response and PANoptosis to promote tumorigenesis. *Cell Rep.* **37**, 109858 (2021).
54. Kuriakose, T. et al. ZBP1/DAI is an innate sensor of influenza virus triggering the NLRP3 inflammasome and programmed cell death pathways. *Sci. Immunol.* **1**, aag2045 (2016).
55. Kwak, H., Lee, E. & Karki, R. DNA sensors in metabolic and cardiovascular diseases: molecular mechanisms and therapeutic prospects. *Immunol. Rev.* **329**, e13382 (2025).
56. Pandey, A., Li, Z., Gautam, M., Ghosh, A. & Man, S. M. Molecular mechanisms of emerging inflammasome complexes and their activation and signaling in inflammation and pyroptosis. *Immunol. Rev.* **329**, e13406 (2025).
57. Moghe, A. et al. Molecular mechanisms of acrolein toxicity: relevance to human disease. *Toxicol. Sci.* **143**, 242–255 (2015).
58. Stockwell, B. R. Ferroptosis turns 10: emerging mechanisms, physiological functions, and therapeutic applications. *Cell* **185**, 2401–2421 (2022).
59. Tang, D., Chen, X., Kang, R. & Kroemer, G. Ferroptosis: molecular mechanisms and health implications. *Cell Res.* **31**, 107–125 (2021).
60. Ru, Q. et al. Iron homeostasis and ferroptosis in human diseases: mechanisms and therapeutic prospects. *Signal Transduct. Target Ther.* **9**, 271 (2024).
61. Chen, X. et al. Translocation of mixed lineage kinase domain-like protein to plasma membrane leads to necrotic cell death. *Cell Res.* **24**, 105–121 (2014).
62. Jacobsen, A. V. et al. HSP90 activity is required for MLKL oligomerisation and membrane translocation and the induction of necroptotic cell death. *Cell Death Dis.* **7**, e2051 (2016).
63. Alarcon, R. A. & Meienhofer, J. Formation of the cytotoxic aldehyde acrolein during in vitro degradation of cyclophosphamide. *Nat. N. Biol.* **233**, 250–252 (1971).
64. Murata, M. et al. Soluble vascular adhesion protein-1 mediates spermine oxidation as semicarbazide-sensitive amine oxidase: possible role in proliferative diabetic retinopathy. *Curr. Eye Res.* **42**, 1674–1683 (2017).
65. Stevens, J. F. & Maier, C. S. Acrolein: sources, metabolism, and biomolecular interactions relevant to human health and disease. *Mol. Nutr. Food Res.* **52**, 7–25 (2008).

66. Tanel, A. & Averill-Bates, D. A. Activation of the death receptor pathway of apoptosis by the aldehyde acrolein. *Free Radic. Biol. Med.* **42**, 798–810 (2007).
67. Roy, J., Pallepati, P., Bettaieb, A., Tanel, A. & Averill-Bates, D. A. Acrolein induces a cellular stress response and triggers mitochondrial apoptosis in A549 cells. *Chem. Biol. Interact.* **181**, 154–167 (2009).
68. Finkelstein, E. I., Nardini, M. & van der Vliet, A. Inhibition of neutrophil apoptosis by acrolein: a mechanism of tobacco-related lung disease?. *Am. J. Physiol. Lung Cell Mol. Physiol.* **281**, L732–L739 (2001).
69. Ou, Y., Wang, S. J., Li, D., Chu, B. & Gu, W. Activation of SAT1 engages polyamine metabolism with p53-mediated ferroptotic responses. *Proc. Natl. Acad. Sci. USA* **113**, E6806–E6812 (2016).
70. Zhao, C. et al. Polyamine metabolism controls B-to-Z DNA transition to orchestrate DNA sensor cGAS activity. *Immunity* **56**, 2508–2522 e2506 (2023).
71. Shi, R., Rickett, T. & Sun, W. Acrolein-mediated injury in nervous system trauma and diseases. *Mol. Nutr. Food Res.* **55**, 1320–1331 (2011).
72. Herbert, A. Z-DNA and Z-RNA in human disease. *Commun. Biol.* **2**, 7 (2019).
73. Su, Z., Yang, Z., Xie, L., DeWitt, J. P. & Chen, Y. Cancer therapy in the necroptosis era. *Cell Death Differ.* **23**, 748–756 (2016).
74. Spiess, P. C., Deng, B., Hondal, R. J., Matthews, D. E. & van der Vliet, A. Proteomic profiling of acrolein adducts in human lung epithelial cells. *J. Proteom.* **74**, 2380–2394 (2011).
75. Dresler, C. M. Is it more important to quit smoking than which chemotherapy is used?. *Lung Cancer* **39**, 119–124 (2003).
76. O'Malley, M., King, A. N., Conte, M., Ellingrod, V. L. & Ramnath, N. Effects of cigarette smoking on metabolism and effectiveness of systemic therapy for lung cancer. *J. Thorac. Oncol.* **9**, 917–926 (2014).
77. Gurney, A. M. & Allam, M. Inhibition of calcium release from the sarcoplasmic reticulum of rabbit aorta by hydralazine. *Br. J. Pharm.* **114**, 238–244 (1995).
78. Oh, S. et al. Integrated NLRP3, AIM2, NLRC4, Pyrin inflammasome activation and assembly drive PANoptosis. *Cell Mol. Immunol.* **20**, 1513–1526 (2023).
79. Han, J. H. et al. NINJ1 mediates inflammatory cell death, PANoptosis, and lethality during infection conditions and heat stress. *Nat. Commun.* **15**, 1739 (2024).
80. Blasi, E., Radzioch, D., Merletti, L. & Varesio, L. Generation of macrophage cell line from fresh bone marrow cells with a myc/raf recombinant retrovirus. *Cancer Biochem. Biophys.* **10**, 303–317 (1989).
81. Man, S. M. et al. IRGB10 liberates bacterial ligands for sensing by the AIM2 and caspase-11-NLRP3 inflammasomes. *Cell* **167**, 382–396 e317 (2016).
82. Pap, E. H. et al. Ratio-fluorescence microscopy of lipid oxidation in living cells using C11-BODIPY(581/591). *FEBS Lett.* **453**, 278–282 (1999).
83. Karki, R. et al. Synergism of TNF-alpha and IFN-gamma triggers inflammatory cell death, tissue damage, and mortality in SARS-CoV-2 infection and cytokine shock syndromes. *Cell* **184**, 149–168 e117 (2021).
84. Karki, R. et al. Concerted activation of the AIM2 and NLRP3 inflammasomes orchestrates host protection against *Aspergillus* infection. *Cell Host Microbe* **17**, 357–368 (2015).
85. Hanzelmann, S., Castelo, R. & Guinney, J. GSVA: gene set variation analysis for microarray and RNA-seq data. *BMC Bioinforma.* **14**, 7 (2013).
86. Al-Mamgani, A. et al. Radiotherapy for T1-2N0 glottic cancer: a multivariate analysis of predictive factors for the long-term outcome in 1050 patients and a prospective assessment of quality of life and voice handicap index in a subset of 233 patients. *Clin. Otolaryngol.* **38**, 306–312 (2013).
87. Boeri, L. et al. Cigarette smoking is associated with adverse pathological response and increased disease recurrence amongst patients with muscle-invasive bladder cancer treated with cisplatin-based neoadjuvant chemotherapy and radical cystectomy: a single-centre experience. *BJU Int.* **123**, 1011–1019 (2019).
88. Browman, G. P. et al. Association between smoking during radiotherapy and prognosis in head and neck cancer: a follow-up study. *Head. Neck* **24**, 1031–1037 (2002).
89. Browman, G. P. et al. Influence of cigarette smoking on the efficacy of radiation therapy in head and neck cancer. *N. Engl. J. Med.* **328**, 159–163 (1993).
90. Chen, A. M. et al. Tobacco smoking during radiation therapy for head-and-neck cancer is associated with unfavorable outcome. *Int. J. Radiat. Oncol. Biol. Phys.* **79**, 414–419 (2011).
91. Platek, A. J. et al. Smoking cessation is associated with improved survival in oropharynx cancer treated by chemoradiation. *Laryngoscope* **126**, 2733–2738 (2016).
92. Rades, D. et al. Evaluation of the impact of smoking and alcohol consumption on toxicity and outcomes of chemoradiation for head and neck cancer. *Anticancer Res.* **43**, 823–830 (2023).

Acknowledgements

We thank all the members of Karki laboratory for their comments and suggestions during the development of this manuscript. We thank Dr. Jinbong Park (Seoul National University) for supplying bone marrow from *Sting*$^{-/-}$ mice. We thank Dr. James M. Murphy (The University of Melbourne, Australia) for providing bone marrow from *Ripk3*$^{-/-}$ and *Mlkl*$^{-/-}$ mice. This work was supported by Creative-Pioneering Researchers Program through Seoul National University (3344-20240032 to R.K.), the National Research Foundation of Korea (NRF) grant funded by the Korea government (MSIT) (RS-2023-00251395 and RS-2025-00554099 to R.K.), the Bio&Medical Technology Development Program of the National Research Foundation (NRF) funded by the Korea government (MSIT) (RS-2024-00440738 to R.K.) and the BK21 Research Fellowship from the Ministry of Education, Science and Technology, Republic of Korea (to R.K.).

Author contributions

Conceptualization: H.B., S.H.M., S.M.M., R.K.; methodology: H.B., S.H.M., M.C., F.Z., C.P., R.M., M.Z., Y.J., W.K., S.K., M.F., J.L., S.P.; investigation: H.B., S.H.M., M.Z., R.K.; reagents: M.Z.; supervision: R.K., S.M.M.; funding acquisition: R.K.; writing–original draft: H.B., S.H.M., S.M.M., R.K.; writing–review & editing: H.B., S.H.M., C.P., R.M., M.Z., S.M.M., R.K.

Competing interests

The authors declare no competing interests.

Additional information

Supplementary information The online version contains supplementary material available at https://doi.org/10.1038/s41467-025-60226-1.

Correspondence and requests for materials should be addressed to Si Ming Man or Rajendra Karki.

Peer review information *Nature Communications* thanks Jing Yang and the other anonymous reviewer(s) for their contribution to the peer review of this work. A peer review file is available.

Reprints and permissions information is available at http://www.nature.com/reprints